Kobe University Repository : Kernel

PDF issue: 2025-12-04

Regulation of lipid synthesis in myelin modulates neural activity and is required for motor learning

Kato, Daisuke ; Aoyama, Yuki ; Nishida, Kazuki ; Takahashi, Yutaka ; Sakamoto, Takumi ; Takeda, Ikuko ; Tatematsu, Tsuyako ; Go, Shiori ;…

(Citation)
Glia,71(11):2591-2608

(Issue Date)
2023-11

(Resource Type)
journal article

(Version)
Version of Record

(Rights)
© 2023 The Authors. GLIA published by Wiley Periodicals LLC.
This is an open access article under the terms of the Creative Commons Attribution License, which permits use, distribution and reproduction in any medium, provided the original work is properly cited.

(URL)
https://hdl.handle.net/20.500.14094/0100483101

Check for updates

Received: 29 December 2022 | Revised: 11 June 2023 | Accepted: 3 July 2023
DOI: 10.1002/glia.24441

GLIA
WILEY

RESEARCH ARTICLE

Regulation of lipid synthesis in myelin modulates neural activity and is required for motor learning

Daisuke Kato[1,2] | Yuki Aoyama[1] | Kazuki Nishida[3] | Yutaka Takahashi[4] | Takumi Sakamoto[4] | Ikuko Takeda[1,2] | Tsuyako Tatematsu[1] | Shiori Go[5] | Yutaro Saito[1] | Shiho Kunishima[1] | Jinlei Cheng[1] | Lingnan Hou[1] | Yoshihisa Tachibana[3] | Shouta Sugio[1] | Reon Kondo[1] | Fumihiro Eto[4,6] | Shumpei Sato[4] | Andrew J. Moorhouse[7] | Ikuko Yao[4,6] | Kenji Kadomatsu[5] | Mitsutoshi Setou[4] | Hiroaki Wake[1,2,8,9,10]

[1]Department of Anatomy and Molecular Cell Biology, Nagoya University Graduate School of Medicine, Nagoya, Japan
[2]Division of Multicellular Circuit Dynamics, National Institute for Physiological Sciences, National Institutes of Natural Sciences, Okazaki, Japan
[3]Division of System Neuroscience, Kobe University Graduate School of Medicine, Kobe, Japan
[4]Department of Cellular and Molecular Anatomy, Hamamatsu University School of Medicine, Hamamatsu, Japan
[5]Institute for Glyco-core Research, Nagoya University, Nagoya, Japan
[6]Department of Biomedical Chemistry, School of Science and Technology, Kwansei Gakuin University, Sanda, Japan
[7]School of Medical Sciences, UNSW Sydney, Sydney, New South Wales, Australia
[8]Center of Optical Scattering Image Science, Kobe University, Kobe, Japan
[9]Department of Physiological Sciences, Graduate University for Advanced Studies, SOKENDAI, Hayama, Japan
[10]Core Research for Evolutional Science and Technology, Japan Science and Technology Agency, Saitama, Japan

Correspondence
Daisuke Kato and Hiroaki Wake, Department of Anatomy and Molecular Cell Biology, Nagoya University Graduate School of Medicine, 65 Tsurumai-cho, Showa-ku, Nagoya 466-8550, Japan.
Email: daikato@med.nagoya-u.ac.jp and hirowake@med.nagoya-u.ac.jp

Funding information
Core Research for Evolutional Science and Technology, Grant/Award Numbers: JPMJCR1755, JPMJCR22P6; Grants-in-Aid for Transformative Research Areas (A), Grant/Award Numbers: 20H05699, 21H05587; Japan Agency for Medical Research and Development, Grant/Award Numbers: JP23gm1410011 h0002, JP22ak0101150; Grants-in-Aid for Young Scientists (A), Grant/Award Number: 26710004; FOREST program, Grant/Award Number: JPMJFR2145; Grants-in-Aid for

Abstract

Brain function relies on both rapid electrical communication in neural circuitry and appropriate patterns or synchrony of neural activity. Rapid communication between neurons is facilitated by wrapping nerve axons with insulation by a myelin sheath composed largely of different lipids. Recent evidence has indicated that the extent of myelination of nerve axons can adapt based on neural activity levels and this adaptive myelination is associated with improved learning of motor tasks, suggesting such plasticity may enhance effective learning. In this study, we examined whether another aspect of myelin plasticity—changes in myelin lipid synthesis and composition—may also be associated with motor learning. We combined a motor learning task in mice with *in vivo* two-photon imaging of neural activity in the primary motor cortex (M1) to distinguish early and late stages of learning and then probed levels of some key myelin lipids using mass spectrometry analysis. Sphingomyelin levels were elevated in the early stage of motor learning while galactosylceramide

Daisuke Kato and Yuki Aoyama are designated as co-first authors.

This is an open access article under the terms of the Creative Commons Attribution License, which permits use, distribution and reproduction in any medium, provided the original work is properly cited.
© 2023 The Authors. *GLIA* published by Wiley Periodicals LLC.

Young Scientists, Grant/Award Number: 20K16574; Nagoya University CIBoG WISE program from MEXT; Grants-in-Aid for Scientific Research on Innovative Areas, Grant/Award Numbers: 25110732, 19H05219, 19H04753; Fostering Joint International Research (B), Grant/Award Number: 20KK0170; Grants-in-Aid for Scientific Research (B), Grant/Award Numbers: 21H02662, 18H02598

levels were elevated in the middle and late stages of motor learning, and these changes were correlated across individual mice with both learning performance and neural activity changes. Targeted inhibition of oligodendrocyte-specific galactosyltransferase expression, the enzyme that synthesizes myelin galactosylceramide, impaired motor learning. Our results suggest regulation of myelin lipid composition could be a novel facet of myelin adaptations associated with learning.

KEYWORDS

calcium imaging, galactosylceramide, lipid synthesis, motor learning, neural activity, oligodendrocyte, sphingomyelin

1 | INTRODUCTION

Myelination of axons by oligodendrocytes is a critical component of neural signaling in the brain, enabling increased action potential conduction speed along axons as well as metabolic support of axons (Fields & Bukalo, 2020; Nave, 2010; Xin & Chan, 2020), and lipids, as the building blocks of myelin, play a critical role in its structure and plasticity (Vaughen et al., 2023). Human magnetic resonance imaging (MRI) diffusion studies have shown that there is a gradual increase in the fractional anisotropy signals into adolescence (Corrigan et al., 2021) and that this increase correlates with myelin levels (Sampaio-Baptista et al., 2013; Sampaio-Baptista & Johansen-Berg, 2017; Scholz et al., 2009). Furthermore, increases in myelination in specific brain regions have been correlated with motor learning and skill acquisition (Sampaio-Baptista & Johansen-Berg, 2017; Scholz et al., 2009). Given that myelin is 70%–80% lipid, an increase in myelination implies an increase in lipid synthesis. Consistently, lipid synthesis, oligodendrocyte proliferation and differentiation, and myelin production are all promoted by neural activity (Gibson et al., 2014; Kato & Wake, 2019; Vaughen et al., 2023; Wake et al., 2011; Wang et al., 2022; Xiao et al., 2016) and lipid synthesis contributes to remote memory (Chen et al., 2020) and behavioral extinction (Huston et al., 2016). Furthermore, targeted disruption of this adaptive myelination can also impair learning. Gene deletion of myelin regulatory factor (MyRF), critical for myelin formation; or overexpressing proteolipid protein 1 (PLP1), which impairs myelin regulation (Tanaka et al., 2009); all lead to reduced motor learning (Kato et al., 2020; McKenzie et al., 2014; Xiao et al., 2016). Abnormal expression of myelin-related genes has also been observed in patients with schizophrenia (Hakak et al., 2001) and reduction in myelin levels is associated with aging and neurodegenerative diseases (Back et al., 2011; Dadar et al., 2022). Given the requirements for both the precise timing of neural activity patterns associated with specific behaviors and increases in synaptic strength within neural circuitry, the link between learning and myelin likely involves an effect on synaptic plasticity and synchrony. The motor learning disruptions seen with impaired myelin regulation are also associated with reduced neural synchrony (Kato et al., 2020). Changes in the lipid composition of myelin can also effect the structure and function of synapses, and thus may contribute to modifications in neural circuitry activity associated with skill acquisition (Fields, 2015).

The current paradigm for myelin-related neural plasticity focuses mainly on changes in the extent of myelination in terms of either the addition of myelin sheaths onto bare axon segments or an increase or decrease in the thickness of existing myelin sheaths (de Faria et al., 2021). The relative contribution of specific myelin lipids, or their regulation, to neural circuitry population activity and plasticity have yet to be investigated during learning. Although not the major lipid species by weight, certain ceramide-derived sphingolipids, including sphingomyelin (SM), galactosylceramide (GalCer), and sulfatides, are abundant in oligodendrocytes and myelin sheaths and are crucial for myelin stability and function (Bosio et al., 1998). The phospholipid sphingomyelin is synthesized in the myelin sheath along with cholesterol and glycolipids (Kister & Kister, 2022). Reductions in the levels of these specific lipid species have been identified in the postmortem brains of patients with multiple system atrophy, a neurodegenerative disease associated with the accumulation of the alpha-synuclein protein within oligodendrocytes (Don et al., 2014). Furthermore, quantifying brain lipid alterations in the shiverer mouse model of dysmyelination and the cuprizone mouse model of reversible demyelination using high-resolution matrix-assisted laser desorption/ionization-imaging mass spectrometry (MALDI-IMS) showed that the levels of sulfatide and other lipids were altered in the white matter (Maganti et al., 2019). Hence, abnormalities in lipid synthesis are associated with myelin-related neural diseases and changes in myelin lipids may also regulate neural activity in non-pathological conditions.

In the current study, we tested this hypothesis using a well-characterized forelimb lever-pulling model of motor learning in combination with *in vivo* two-photon Ca^{2+} imaging of neural circuitry changes. Motor learning was divided into three phases, and MALDI-IMS was used to analyze brain samples obtained in each phase. This enabled us to map out any changes in specific key myelin lipid species in the primary motor cortex (M1) that were correlated with neural circuitry changes during learning. Our data demonstrated distinct increases in specific SM and GalCer species at different stages of motor learning. Furthermore, targeted ablation of GalCer synthesizing enzymes disrupted skill acquisition, supporting the notion that a dynamic increase in myelin lipid synthesis is required for motor skill acquisition.

10981136, 2023, 11, Downloaded from https://onlinelibrary.wiley.com/doi/10.1002/glia.24441 by Kobe University, Wiley Online Library on [14/09/2023]. See the Terms and Conditions (https://onlinelibrary.wiley.com/terms-and-conditions) on Wiley Online Library for rules of use; OA articles are governed by the applicable Creative Commons License

2 | MATERIALS AND METHODS

2.1 | Animals and head plate fixation surgery

All experiment protocols were approved by the Institutional Animal Care and Use Committee of Kobe University Graduate School of Medicine, Nagoya University Graduate School of Medicine, and Hamamatsu University School of Medicine and were conducted according to the guidelines of the National Institutes of Health Guide for the Care and Use of Laboratory Animals. Wild-type (WT) C57BL/6 mice (6–8 weeks old) were used for the experiments. The animals were given free access to food and water and were maintained on a 12 h light/dark cycle. Mice were anesthetized by intraperitoneal injection (i.p.) of ketamine (74 mg/kg) and xylazine (10 mg/kg). The skin was disinfected using 70% alcohol, the skull was exposed and cleaned, and a head plate was firmly attached using dental cement (G-CEM ONE; GC, Tokyo, Japan). The surface of the intact skull was subsequently coated with an acrylic-based dental adhesive resin cement (Super-Bond; Sun Medical, Shiga, Japan) to prevent drying, as previously described (Kato et al., 2020). The mice were allowed to recover for 1 day before surgery and viral vector injection.

2.2 | Targeted inhibition of GalCer synthesis

Short-hairpin RNA (shRNA) were designed and synthesized by Vector-Builder, Inc. (Table 1) and used for targeted inhibition of the enzyme ceramide galactosyltransferase (CGT) to reduce GalCer synthesis. Inhibitory efficiency was validated *in vitro* using the CMT 167 cell line (ATCC, Manassas, VA), which was originally derived from C57BL/6J mice and is known to express CGT. CGT levels were measured using quantitative reverse transcription polymerase chain reaction (RT-qPCR). The verified target shRNA sequences were introduced into WT mice by injection of the corresponding adeno-associated virus (AAV) vector into the brain.

2.3 | AAV injection and surgery

AAV injection and surgery were performed 2 to 3 weeks prior to the experiments. Dexamethasone sodium phosphate (1.32 mg/kg) was administered intraperitoneally 1 h before surgery to prevent cerebral edema. Under 1% isoflurane anesthesia, a ~ 2 mm diameter circular craniotomy (circle centered at ~0.2 mm anterior and ~ 1 mm lateral from the bregma) was performed over the left M1 as previously described (Kato et al., 2020). A Ca^{2+} fluorophore (GCaMP6f) coupled to a neural promoter was expressed to visualize neural activity in M1 layer 2/3 (L2/3) neurons. A total of 1 μL AAV (AAV1-Syn-GCaMP6f, Penn Vector Core; 9.0×10^{12} vector genomes/ml) solution was injected through a glass pipette (tip diameter, 25–30 μm). For experiments to determine the cell specificity of the myelin-associated glycoprotein (MAG) promoter in the AAV vectors, AAV8-MAG-mScarlet (0.5 μL, 8.8×10^{13} vector genomes/ml) was injected into the white matter (with coordinates targeting the white matter beneath the M1: AP = 0.2 mm; ML = 1.0 mm; DV = −1.2 mm from the bregma). To silence the expression of CGT in oligodendrocytes, validated CGT shRNA sequences were similarly injected into the white matter (0.5 μL AAV solutions of either shRNA against CGT [AAV8-MAG-shRNA1, 8.2×10^{13} vector genomes/ml or AAV8-MAG-shRNA2, 5.8×10^{13} vector genomes/ml] or scrambled RNA [AAV8-MAG-scrambled RNA, 4.5×10^{13} vector genomes/ml]). The pipette was maintained in place for an additional 5 min before removal. After the injection, 2% (wt/vol) agarose L (Nippon Gene, Tokyo, Japan) in saline was placed over the craniotomy; then, a glass window comprising two coverslips (diameter, 2 and 4.5 mm; Matsunami Glass, Osaka, Japan) joined using ultraviolet curable adhesive (NOR-61, Norland) was pressed onto the agarose surface and the edges were sealed using dental cement (G-CEM ONE; GC, Tokyo, Japan) and dental adhesive resin cement (Super-Bond; Sun Medical, Shiga, Japan). The mice were then returned to their cages for recovery.

TABLE 1 Nucleotide sequences of the shRNAs used in this study.

Target	shRNA sequence
shCGT1	5′-CCATGTGTAAATGCTTATTT-3′
shCGT2	5′-GCTCAGAAGTTATCGGAAATT-3′
scrambled	5′-CCTAAGGTTAAGTCGCCCTCG-3′

2.4 | Lever-pull task

A previously described voluntary (self-initiated) forelimb movement task was modified for use in this study (Kato et al., 2020). Mice with attached head plates were habituated to the task apparatus for 1 h per day for 2 days prior to the start of the experiment. After habituation, mice were deprived of water in their home cages and maintained at 85% of their normal body weight throughout the experiment. Each mouse was trained to perform the voluntary right-forelimb movement for 1 h per day for 12 training days. When a mouse pulled the lever and held it there for 600 ms, it was rewarded with a 4 μL drop of water from a spout near its mouth. If a lever-pull failed to be held for the full 600 ms, the lever returned to its starting position and the mice could pull it again at any time. A program written in LabVIEW (National Instruments, Austin, TX) was used to control the timing of the reward, lever return, and lever immobilization, and also to continuously monitor the lever position. The behavior and performance of the mice were monitored using an infrared video camera. After each training session, mice were allowed access to 1 mL of water. Twenty-one WT mice were used for these experiments (Group A: $n = 5$ mice, Group B: $n = 7$ mice, Group C: $n = 9$ mice; Figures 1–3).

2.5 | Two-photon imaging

Two-photon images of the left M1 were captured during the lever-pull task (on days 2, 4, 7, and 12) using an LSM 7 MP system (Carl Zeiss, Oberkochen, Germany) with a 10× objective (XLPlan, Carl Zeiss; numerical aperture [NA]: 0.5) and a mode-locked Ti:sapphire laser (Mai Tai HP; Spectra-Physics, Santa Clara, CA) at a

10981136, 2023, 11, Downloaded from https://onlinelibrary.wiley.com/doi/10.1002/glia.24441 by Kobe University, Wiley Online Library on [14/09/2023]. See the Terms and Conditions (https://onlinelibrary.wiley.com/terms-and-conditions) on Wiley Online Library for rules of use; OA articles are governed by the applicable Creative Commons License

wavelength of 950 nm. Fluorescence signals were obtained using GaAsP photomultiplier tubes (Hamamatsu Photonics, Shizuoka, Japan). The laser intensity used for imaging was 20–30 mW. The imaged field area was 848.54 μm × 848.54 μm at a depth of 150–200 μm from the cortical surface. Pixel size was 1.657 μm. Continuous 1000-frame imaging was repeated in each field (frame duration: 390 ms). Lever positions and solenoid signals (that detected successful lever-pulls) were also recorded simultaneously.

2.6 | Image analysis of two-photon imaging

Two-photon images were analyzed using an ImageJ plug-in (1.37v; NIH) and scripts written in MATLAB (MathWorks, Natick, MA). Images were corrected for focal/XY plane displacement using the TurboReg and StackReg ImageJ plug-ins (Thévenaz et al., 1998). To quantify neural activity in the M1, regions of interest (ROIs) in L2/3 were defined using an automated algorithm (CaImAn; http://github.com/simonsfoundation/) that

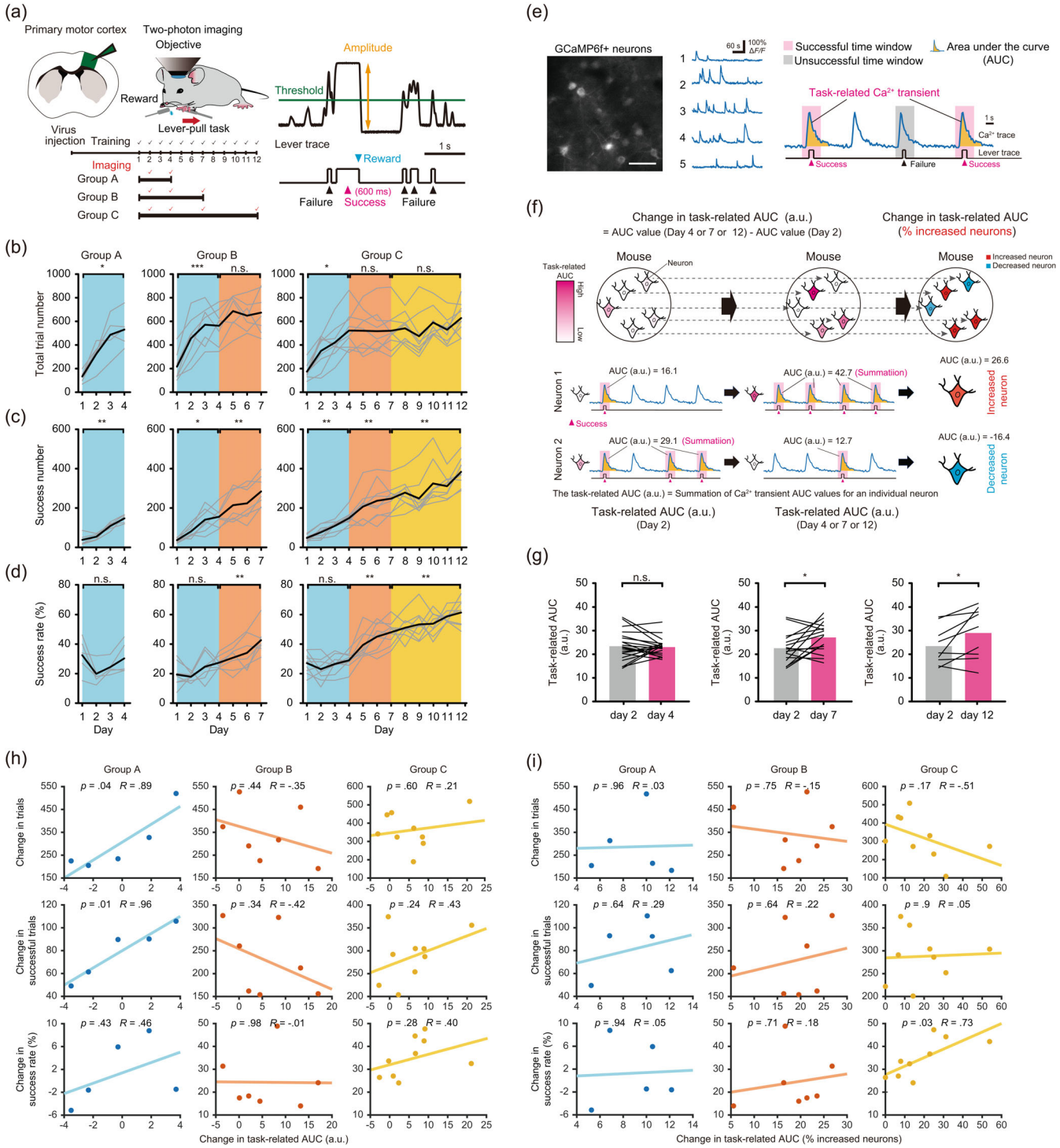

FIGURE 1 Legend on next page.

10981136, 2023, 11, Downloaded from https://onlinelibrary.wiley.com/doi/10.1002/glia.24441 by Kobe University, Wiley Online Library on [14/09/2023]. See the Terms and Conditions (https://onlinelibrary.wiley.com/terms-and-conditions) on Wiley Online Library for rules of use; OA articles are governed by the applicable Creative Commons License

determines an ROI as a discrete region with a change in fluorescence intensity at some stage during the analysis. Completely silent neurons (and/or those without GCaMP6f expression) will not be detected using this approach. The numbers of analyzed ROIs were as follows: Group A: WT mice (five fields from five mice on each day), 275 on day 2, 467 on day 4; Group B (seven fields from seven mice on each day), 405 on day 2, 557 on day 4, 499 on day 7; Group C (nine fields from nine mice on each day), 260 on day 2, 359 on day 4, 388 on day 7, 299 on day 12. To detect and analyze Ca^{2+} transients, baseline fluorescence (F_0) was defined as the 35th percentile of the total fluorescence intensity histogram obtained during the imaging period. A Ca^{2+} transient was defined as $\Delta F/F_0$ ($\Delta F = F - F_0$), where F is the instantaneous fluorescent signal and F_0 is the baseline fluorescence, when ΔF exceeded two standard deviations (SDs) of F_0 (Kato et al., 2020; Tian et al., 2009). To normalize the changes in the Ca^{2+} transients, we subtracted the mean value of the Ca^{2+} transient for each ROI and divided it by the deviation to account for different degrees of variability (= z-score Ca^{2+} transient) (Sun et al., 2019). The area under the curve (AUC) was calculated for each z-score Ca^{2+} transient and summed for individual ROIs. Lever-related Ca^{2+} transients were defined as those occurring between 0.8 s before and 1.6 s after the start of lever-pulling, and were divided into successful (task-related Ca^{2+} transients) or unsuccessful (unrelated to the task) lever-pulls. Only imaging sessions with more than three successful lever-pulls were analyzed.

2.7 | MALDI-IMS of white matter samples

Coronal sections (thickness, 10 μm) were cut from frozen brains using a Leica CM3050S cryostat (Leica Microsystems, Wetzlar, Germany) and obtained serially from ~0.1 to 0.4 mm posterior to the bregma. Sections were mounted on indium tin oxide-coated glass slides (Matsunami Glass Ind., Osaka, Japan) and sprayed with a matrix solution (40 mg/mL 2,5-dihydroxybenzoic acid, 20 mM potassium acetate, 0.2% trifluoroacetic acid in 50% methanol) using a TM-sprayer (HTX Technologies, Chapel Hill, NC) (Sugimoto et al., 2015). A solariX XR FT-ICR mass spectrometer (Bruker Daltonics, Bremen, Germany) was used for MALDI-IMS. Mass spectra were acquired in positive ion mode to detect lipid species of interest in the *m/z* 688–950 range. The laser was operated at 1000 Hz, the laser spot size was 50 μm, and the lateral resolution was 100 μm, with 50 shots collected per pixel. Data were visualized using flexImaging (Bruker Daltonics). Lipids were identified by accurate mass referencing to the LIPID MAPS and SwissLipids databases. Analysis were performed using scripts written in MATLAB.

2.8 | Lipid extraction and standard solution preparation

To prepare the lipid standard solutions, we added acetonitrile/isopropanol (1:9) to each standard lipid powder [Glucosylceramid (GlcCer)(18:1/24:1) and GalCer(18:1/24:0)] in a glass tube to give a concentration of 250 μg/mL, and sonicated this solution until completely dissolved. The two standard lipid solutions were then mixed and diluted further with acetonitrile in a glass vial (L.E. Technologies, Inc.) to a concentration of 10 μg/mL. These diluted standards were then stored at −80°C until use. To extract lipids from frozen brain samples, we employed the modified Bligh-Dyer method. First, we added water to the frozen tissue sample in a glass tube (1 mL per 4 mg) and homogenized the mixture using a digital homogenizer (HK-1, AS ONE Corporation). The homogenate was collected

FIGURE 1 Changes in behavior and neural circuitry activity during motor learning. (a) Diagrammatic representation of the motor learning experiments. Head-restrained mice were trained to perform self-initiated right-forelimb movements. If the mice pulled the lever and held it for 600 ms, a water reward followed. Three separate mice groups representing different motor learning periods (Group A [$n = 5$]; days 1–4, Group B [$n = 7$]; days 1–7, and Group C [$n = 9$]; days 1–12) were examined, with brains excised for lipid analysis at the end of each period. (b–d) Plots of the three different motor behavior parameters over days of training in groups A (left panels), B (middle panels), and C (right panels). Data for each mouse are shown in gray with mean data in bold. One-way ANOVA followed by Tukey's test; $^*p < .05$, $^{**}p < .01$, $^{***}p < .001$, n.s., non-significant. (b) Total trial number: Group A: $F_{3,16} = 4.66$, $p = .018$ (day 1 vs. day 4); Group B: $F_{6,42} = 17.18$, $p = 8.00 \times 10^{-4}$ (day 1 vs. day 4), $p = .28$ (day 4 vs. day 7); Group C: $F_{11,96} = 16.68$, $p = .012$ (day 1 vs. day 4), $p = .99$ (day 4 vs. day 7), $p = .69$ (day 7 vs. day 12); (c) Number of successful trials: Group A: $F_{3,16} = 2.11$, $p = 8.20 \times 10^{-3}$ (day 1 vs. day 4); Group B: $F_{6,42} = 8.23$, $p = .011$ (day 1 vs. day 4), $p = 2.70 \times 10^{-3}$ (day 4 vs. day 7); Group C: $F_{11,96} = 16.24$, $p = 1.30 \times 10^{-3}$ (day 1 vs. day 4), $p = 6.90 \times 10^{-3}$ (day 4 vs. day 7), $p = 1.90 \times 10^{-3}$ (day 7 vs. day 12); (d) Success rate (success number / total trials, %); Group A: $F_{3,16} = 5.23$, $p = .97$ (day 1 vs. day 4); Group B: $F_{6,42} = 2.20$, $p = .55$ (day 1 vs. day 4), $p = 7.30 \times 10^{-3}$ (day 4 vs. day 7); Group C: $F_{11,96} = 5.02$, $p = 1.00$ (day 1 vs. day 4), $p = 2.10 \times 10^{-3}$ (day 4 vs. day 7), $p = 7.60 \times 10^{-3}$ (day 7 vs. day 12). (e) Representative image of L2/3 M1 neurons expressing GCaMP6f (left panel), Ca^{2+} traces of five representative neurons (middle panel), and definition of task-related Ca^{2+} transients and the area under the curve (AUC) of a Ca^{2+} transient (right panel). Scale bar, 50 μm. (f) Definition of the parameters used to relate neural activity to behavioral (task) performance. Changes in the task-related activity were quantified by the difference in summed task-related Ca^{2+} transients (summed AUCs) between that on day 2 and either day 4, day 7, or day 12, with mean values calculated for each mouse. Neurons with an increase in task-related AUC were defined as increased neurons, and neurons with a decrease in task-related AUC were defined as decreased neurons. The percentages of increased neurons in each individual mouse [task-related AUC (% increased neurons)] during the training period were quantified. (g) The mean summed task-related AUC (a.u.) on days 2, 4, 7, 12 were compared ($p = .76$ [day 2 vs. day 4], $p = .023$ [day 2 vs. day 7], $p = .046$ [day 2 vs. day 12], paired *t*-test). Each plotted line represents an individual mouse. $^*p < .05$, n.s., non-significant. (h) Correlation plots between change in task-related AUC and change in task performance in each mouse group (change from day 2 to day 4 [Group A, blue], from day 2 to day 7 [Group B, orange], and from day 2 to day 12 [Group C, yellow]). Each dot represents data for an individual mouse. (i) Correlation plots between change in task-related AUC (% increased neurons) and change in task performance in each mouse group (change from day 2 to day 4 [Group A, blue], from day 2 to day 7 [Group B, orange], and from day 2 to day 12 [Group C, yellow]). Each dot represents data for an individual mouse.

10981136, 2023, 11, Downloaded from https://onlinelibrary.wiley.com/doi/10.1002/glia.24441 by Kobe University, Wiley Online Library on [14/09/2023]. See the Terms and Conditions (https://onlinelibrary.wiley.com/terms-and-conditions) on Wiley Online Library for rules of use; OA articles are governed by the applicable Creative Commons License

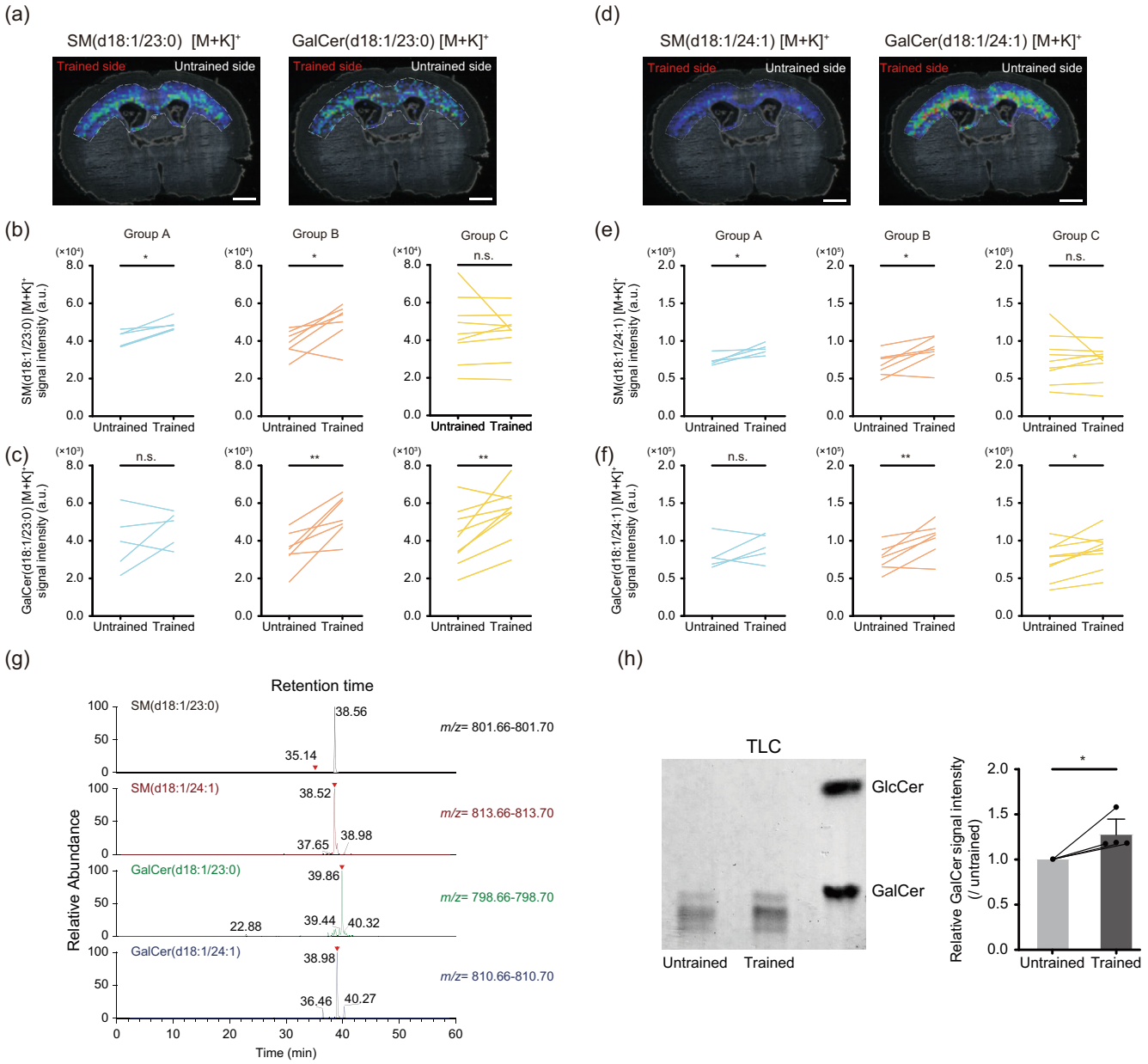

FIGURE 2 Changes in myelin lipid levels during motor learning. (a) Representative images of SM (d18:1/23:0) and GalCer (d18:1/23:0) levels in tissue sections from an early (Group A) and late phase (Group C) mouse, respectively. Scale bar, 500 μm. (b, c) In the early (Group A) and middle (Group B) stages, there was a significant increase in the intensity of SM (d18:1/23:0) in left (trained) white matter beneath M1 relative to that in the right (untrained) white matter beneath M1 after motor learning. In contrast, in the middle and late (Group C) phases, trained mice showed a higher intensity of GalCer (d18:1/23:0) in the left (trained) white matter beneath M1 relative to that in right (untrained) white matter beneath M1. Each line is plotted for an individual mouse. Paired *t*-test. $^{*}p < .05$, $^{**}p < .01$, n.s., non-significant. (d) Representative images showing SM (d18:1/24:1) and GalCer (d18:1/24:1) levels in tissue sections from the early (Group A) and late (Group C) phases. Scale bar, 500 μm. (e, f) Changes in SM (d18:1/24:1) and GalCer (d18:1/24:1) levels across the different phases of learning were similar to those shown in panels (b) and (c) for the shorter SM and GalCer species. Each line is plotted for an individual mouse. Paired *t*-test. $^{*}p < .05$, $^{**}p < .01$, n.s., non-significant. (g) Representative LC–MS/MS spectrum of brain samples obtained after 12 days of motor learning. Multiple isomers with corresponding masses were detected for SM (d18:1/23:0) and GalCer (d18:1/23:0 and d18:1/24:1), but not for SM (d18:1/24:1). The maximum relative abundances of isomers with masses corresponding to GalCer (d18:1/23:0) and GalCer (d18:1/24:1) showed 39.9 and 39.0 min of retention times, respectively. (h) Representative TLC image of brain samples obtained after 12 days motor learning with standards for GalCer and GlcCer shown (left panel). Quantitative analysis of relative TLC GalCer mean expression from four brain samples (right panel). Paired *t*-test. $^{*}p < .05$.

and transferred to glass centrifuge tubes (Iwaki) to which chloroform and methanol (FUJIFILM Wako Pure Chemical) were added using glass tips (Corning), and the mixture was vortexed. After 10 min at room temperature (RT), we added more chloroform and vortexed the mixture again. Finally, we added acetic acid (Wako) and gave a final vortex, before centrifugation at 1000 rpm for 15 min, and then

10981136, 2023, 11, Downloaded from https://onlinelibrary.wiley.com/doi/10.1002/glia.24441 by Kobe University, Wiley Online Library on [14/09/2023]. See the Terms and Conditions (https://onlinelibrary.wiley.com/terms-and-conditions) on Wiley Online Library for rules of use; OA articles are governed by the applicable Creative Commons License

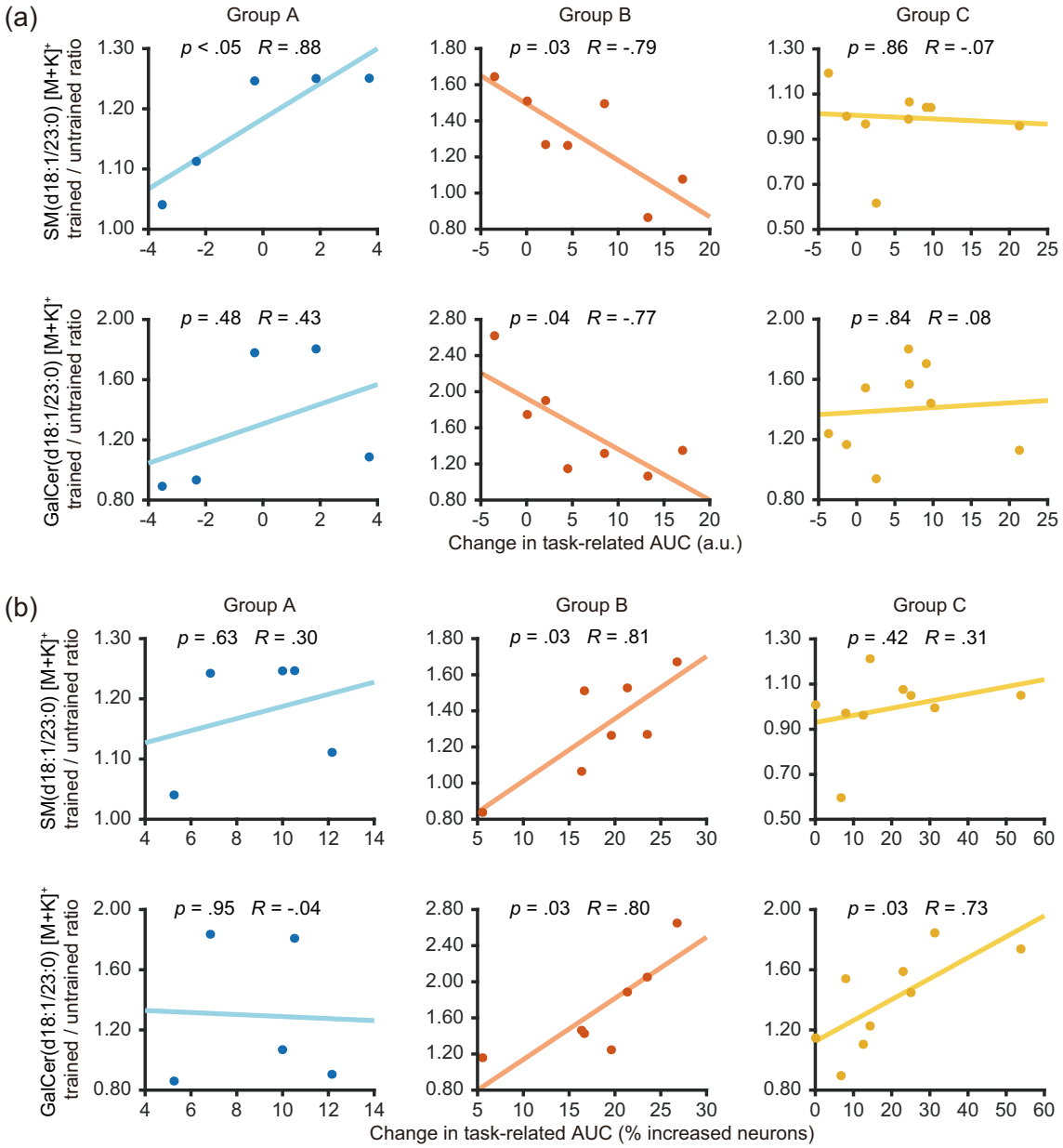

FIGURE 3 Correlations between neural activity pattern changes and lipid levels (SM [d18:1/23:0] and GalCer [d18:1/23:0]) at different stages of motor learning. (a) Correlation plots between changes in task-related AUC (change from day 2 to day 4 [Group A, blue], from day 2 to day 7 [Group B, orange], and from day 2 to day 12 [Group C, yellow]) and changes in SM (d18:1/23:0) (upper panels) and GalCer (d18:1/23:0) (lower panels) levels during early (left), middle (center) and late (right) stages of motor learning. Each dot represents an individual mouse. Pearson's correlation test. *$p < .05$. n.s., non-significant. (**b**) Correlation plots between changes in the proportion of neurons with increased task-related AUCs (change from day 2 to day 4 [Group A, blue], from day 2 to day 7 [Group B, orange], and from day 2 to day 12 [Group C, yellow]) and changes in SM (d18:1/23:0) (upper panels) and GalCer (d18:1/23:0) (lower panels) levels during early (left), middle (center) and late (right) stages of motor learning. Each dot represents an individual mouse. Pearson's correlation test. *$p < .05$. n.s., non-significant.

carefully removing the organic (bottom) layer, and drying it in a Spin Dryer Standard VC-96R concentrator connected to a VA-500R (TAITEC) cold trap, and finally storing this extracted and dried sample at −80°C until use (Takanashi et al., 2020). The ratio of water to chloroform to methanol to acetic acid in these brain samples was 0.8:2:2:1.

2.9 | Liquid chromatography/mass spectrometry of white matter

Lipids were dissolved in acetonitrile to a final concentration equivalent to 20 mg/mL of frozen tissue and transferred into a glass vial (L.E. Technologies, Inc.) designed for liquid chromatography/mass

10981136, 2023, 11, Downloaded from https://onlinelibrary.wiley.com/doi/10.1002/glia.24441 by Kobe University, Wiley Online Library on [14/09/2023]. See the Terms and Conditions (https://onlinelibrary.wiley.com/terms-and-conditions) on Wiley Online Library for rules of use; OA articles are governed by the applicable Creative Commons License

spectrometry (LC–MS) analysis with a glass insert (Systech). The lipids and standard mixture were then analyzed using a Q Exactive™ Hybrid Quadrupole-Orbitrap™ mass spectrometer connected to an Ultimate 3000 system (Thermo Scientific). A 10 μL sample of brain lipids or a 2 μL sample of the lipid standards was injected into an Accucore 120 C18 column (150 mm × 2.1 mm, 3 μm) (Thermo Scientific) for separation. The mobile phase was composed of part A, which consisted of water-acetonitrile-methanol (2:1:1 vol/vol/vol), 5 mM ammonium formate, and 0.1% formic acid, and part B, which consisted of acetonitrile-isopropanol (1:9 vol/vol), 5 mM ammonium formate, and 0.1% formic acid. The mobile phase flow rate was set at 300 μ/min using a linear-gradient program, starting with 20% solvent B and increasing linearly to 100% B over 50 min, then holding at 100% B for 10 min before reducing linearly to 20% B between 60 min and 60.1 min, and ending with 20% B over the last 10 min. The total runtime was 70 min. The MS instrument parameters were as follows: probe heater temperature, 350°C; S-lens RF level, 50; capillary temperature, 250°C; auxiliary gas flow rate, 15; sheath gas flow rate, 50; sweep gas flow rate, 0; spray voltage in positive mode, 3.5 kV and in negative mode, 2.5 kV. The mass spectra recording conditions were as follows: AGC target, 1e6; mass resolving power, 70,000 (FWHM); recorded *m/z* range, 220–2000; maximum injection time, 100 ms. The Xcalibur v3.0 software (Thermo Scientific) was used to obtain spectral data. MS/MS spectra were acquired using the precursor ion corresponding to the *m/z* value of each target lipid molecule (SM species d18:1/23:0 and d18:1/24:1 and GalCer species d18:1/23:0 and d18:1/24:1), and the structures were identified using the product ion spectra.

2.10 | Thin-layer chromatography

Briefly, total cell lipids were extracted using chloroform/methanol (1:1 and 1:2, vol/vol) and concentrations measured using the BCA assay. After alkaline methanolysis (with 1 N NaOH in methanol), desalting was performed using a Sep-Pak C18 cartridge. Lipids were spotted on borate-impregnated HPTLC plates, developed using a chloroform/methanol/water (80:30:4, vol/vol/vol) solution, and visualized using orcinol/sulfuric acid staining (Go et al., 2017; Gupta et al., 2010). Image analyses were performed using CS analyzer (Atto).

2.11 | Real-time PCR

For mRNA levels quantification, total RNA was extracted from CMT 167 cells or white matter samples using the RNeasy Plus Mini kit (Qiagen, Hilden, Germany). First-strand complementary DNA (cDNA) was synthesized from total RNA using the Transcriptor First Strand cDNA Synthesis Kit (Roche Diagnostics, Mannheim, Germany). PCR was performed using the QuantStudio 1 system (Thermo Fisher, MA) and the FastStart Essential DNA Green Master mix (Roche Diagnostics). Amplification results were analyzed using the QuantStudio 1 software and then normalized based on the expression level of glyceraldehyde-3-phosphate dehydrogenase (Gapdh) mRNA in each sample. The following pairs of primers were used:

CGT forward: 5′-TGAAGGAGAGCTGTATGATGCC-3′ and reverse: 5′-TGATGGACAGCAGAACGGAG-3′; *MBP* were forward: 5′-GAAGG CAGGTGATGGTTGA-3′ and reverse: 5′-AACACTCCCGTGGGACAATC; *Gapdh* were forward: 5′-GGGCTGGCATTGCTCACA-3′ and reverse: 5′-TGTAGCCGTATTCATTGTCATACCA-3′. For the experiments on inhibition of GalCer synthesis during motor learning (Figure 5), 15 WT mice were used (five WT mice each in the scrambled RNA, shRNA1, and shRNA2 groups).

2.12 | Western blotting

Mice injected with AAV vectors for shRNA against CGT (AAV8-MAG-shRNA1 or AAV8-MAG-shRNA2) or scrambled RNA (AAV8-MAG-scrambled RNA) were deeply anesthetized using ketamine (74 mg/kg, i.p.) and xylazine (10 mg/kg, i.p.) and transcardially perfused with ice-cold phosphate-buffered saline (PBS). After removal of the brain, the white matter under the M1 on the side which received the AAV vector injection, was dissected and homogenized in N-PER™ Neuronal Protein Extraction Reagent (Thermo Scientific, Rockford, IL) with a protease inhibitor (Nacalai Tesque, Japan). Following a 10 min incubation on ice, the homogenate was centrifuged at 10,000 × g (10 min at 4°C). Protein concentration was determined using the Pierce™ BCA Protein Assay Kit (Thermo Scientific). After electrophoresis of supernatant samples (3 μg protein per sample) on 4%–20% Mini-PROTEAN® TGX™ gels (Bio-Rad Lab, Tokyo, Japan), proteins were transferred to a Trans-Blot Turbo 0.2-micron PVDF membrane (Bio-Rad Lab, Tokyo, Japan). The membranes were incubated with anti-Ugt8a (rabbit; Proteintech, 19,782-2-AP; 1:500) and anti-GAPDH (rabbit; Cell Signaling, D16H11; 1:3000) antibodies, and then with the appropriate HRP-conjugated anti-rabbit antibody (Ugt8a: donkey; Invitrogen, 31,458; 1:10,000, diluted in Can Get Signal Solution 2 [TOYOBO] and GAPDH: diluted in 5% skim milk in Tris buffered saline with Tween 20). Immunoreactive bands were visualized using the SuperSignal™ West Dura Extended Duration Substrate (Thermo Scientific) for Ugt8a and the Immobilon Classico Western HRP substrate (Millipore) for GAPDH, followed by image acquisition and analyses using the iBright™ CL1500 Imaging System (Thermo Scientific).

2.13 | Immunohistochemistry

Mice were deeply anesthetized using ketamine (74 mg/kg, i.p.) and xylazine (10 mg/kg, i.p.) and transcardially perfused with a 4% paraformaldehyde in PBS. Fixed brain tissues were equilibrated in 30% sucrose solution in PBS and sliced into 30 μm-thick sections using a microtome (Leica Microsystems, Wetzlar, Germany). After blocking for 1 h in PBS with 10% normal goat serum and 0.3% Triton-X at RT, brain sections were incubated overnight at 4°C with primary antibodies in the same PBS solution, followed by 1 h incubation with secondary antibody at RT, before mounting on glass slides

10981136, 2023, 11, Downloaded from https://onlinelibrary.wiley.com/doi/10.1002/glia.24441 by Kobe University, Wiley Online Library on [14/09/2023]. See the Terms and Conditions (https://onlinelibrary.wiley.com/terms-and-conditions) on Wiley Online Library for rules of use; OA articles are governed by the applicable Creative Commons License

with VECTASHIELD Antifade Mounting Medium with DAPI (Vector Laboratories, Newark, CA). Imaging was performed using an LSM 510 META confocal microscope (Carl Zeiss, Oberkochen, Germany) with a 20× objective (Carl Zeiss; NA: 1.0) (Figure 4o; 1024 × 1024 pixels, 0.313 μm/pixel, 5.0 μm Z-step) or a FV3000 confocal microscope (Olympus) with a 10× objective (Olympus; NA: 0.3) and a 60× oil-immersion objective (NA: 0.9). The following antibodies were used: anti-Ugt8a (rabbit; Proteintech, 19,782-2-AP; 1:500), anti-adenomatous polyposis coli (clone CC1) (mouse; Calbiochem, OP80; 1:500), anti-NeuN (mouse; Millipore, MAB377; 1:500), anti-S100β (rabbit; Abcam, ab52642; 1:1000), anti-myelin basic protein (MBP) (mouse; BioLegend, clone SMI 99; 1:100), donkey anti-rabbit Alexa 488 (Abcam, ab150073; 1:500), goat anti-mouse Alexa 594 (Abcam, ab150116; 1:500), donkey anti-goat Alexa

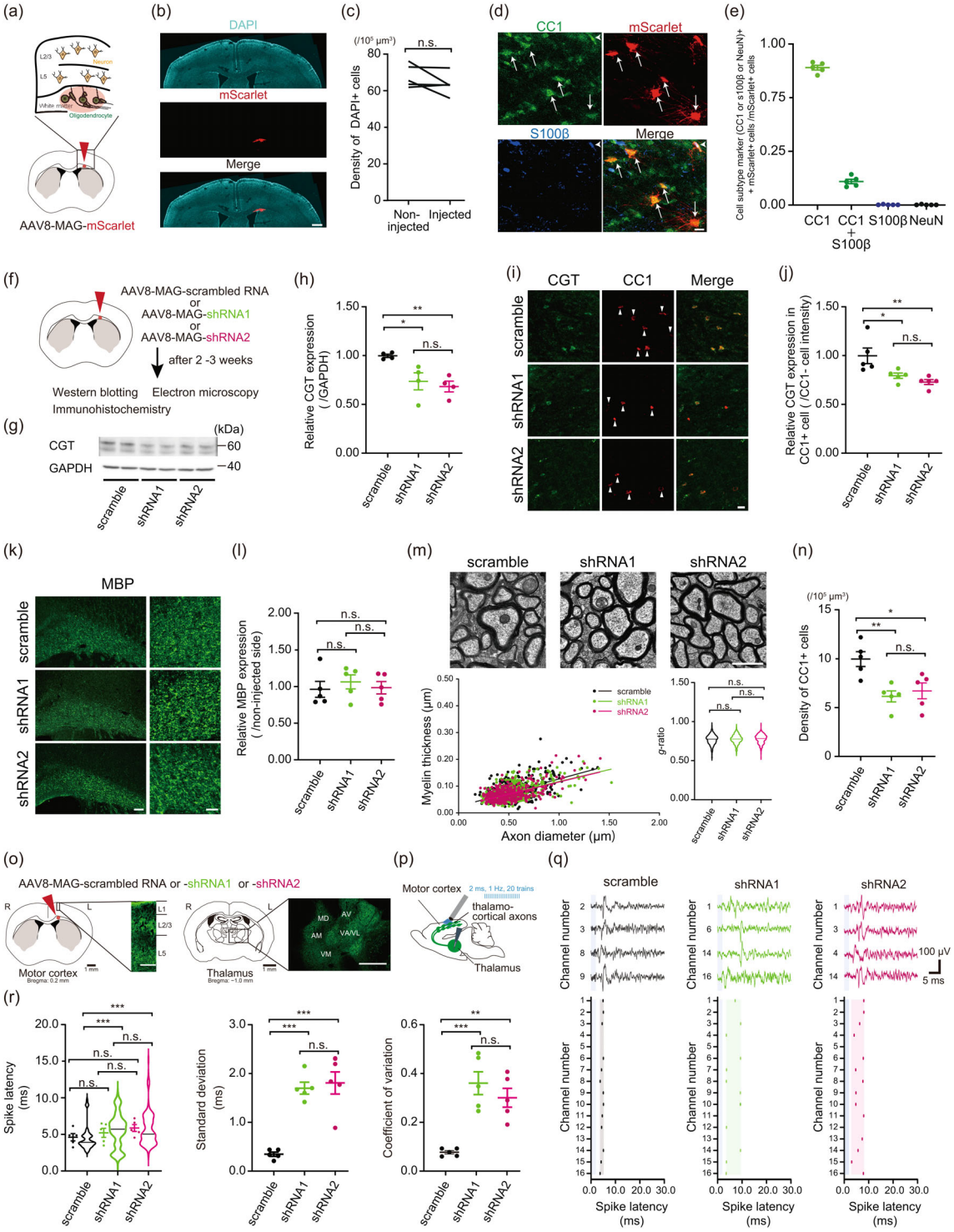

FIGURE 4 Legend on next page.

10981136, 2023, 11, Downloaded from https://onlinelibrary.wiley.com/doi/10.1002/glia.24441 by Kobe University, Wiley Online Library on [14/09/2023]. See the Terms and Conditions (https://onlinelibrary.wiley.com/terms-and-conditions) on Wiley Online Library for rules of use; OA articles are governed by the applicable Creative Commons License

488 (Abcam, ab150129; 1:500), donkey anti-rabbit Alexa 594 (Abcam, ab150076; 1:500), donkey anti-mouse Alexa 405 (Abcam, ab175658; 1:500), and donkey anti-mouse Alexa 647 (Abcam, ab15017; 1:500). The number of DAPI positive cells (Figure 4b,c) and CC1 positive cells (Figure 4i,n) were determined from confocal 3D image data (DAPI; 512 × 512 pixels, 2.486 μm/pixel, 5 μm Z-step, 5 slices, CC1; 1024 × 1024 pixels, 2.486 μm/pixel, 5 μm Z-step, 5 slices). Images were taken under the following conditions: for experiments to determine cell type specificities of the MAG promoter (Figure 4d,e); 512 × 512 pixels, 0.414 μm/pixel, 0.5 μm Z-step; for experiments to examine the expression level of CGT (Figure 4i,j) and MBP (Figures 4k,l and S2b); 1024 × 1024 pixels, 2.486 μm/pixel, 5 μm Z-step. Image analysis was performed using Fiji or Imaris (ver 9.8.2 or ver stitcher 9.7.2) (Oxford Instruments, UK).

2.14 | Electrophysiology

To examine the effect of CGT inhibition on axonal action potential propagation, AAV8-MAG-scrambled RNA (0.5 μL) or AAV8-MAG-shRNA (shRNA1 or shRNA2, 0.5 μL) was injected into the left thalamocortical white matter projection tracts beneath the M1 (0.2 mm anterior and 1 mm lateral from the bregma and 1.2 mm below the pia) and AAV1-Syn- channelrhodopsin (H134R)-EYFP (ChR2; 0.5 μL, 2.11×10^{13} vector genomes/ml) was injected into the left thalamic motor nucleus (1 mm posterior and 1 mm lateral from the bregma and 3.2 mm below the pia). Two to three weeks later, electrophysiological experiments were conducted under 0.8%–1% isoflurane anesthesia to measure spikes evoked by optogenetic activation of thalamocortical projections. Antidromic spikes were recorded using a 16-channel planar electrode array inserted into the thalamic nuclei following optogenetic stimulation of the cortex via a fiber-optic cable placed close to the cortical surface exposed by a craniotomy. Stimulation was twenty 473 nm (Thorlabs, Newton, NJ) pulses (2 ms each, 1 Hz) with a power at the fiber-optic tip of approximately 10 mW. Stable spike responses during optogenetic stimulation that appeared consistently (at least in response to 10 stimuli) and that occurred within 30 ms of the stimulus onset, and had low spike jitter (<0.3 ms) were defined as antidromic spikes (Ciocchi et al., 2015; Kato et al., 2020) and further analyzed. To assess the temporal dispersion of the antidromic spike latency, the SD and coefficient of variation were calculated using units that were simultaneous detected from two or more different channels in the 16-channel array (and also satisfied the selection criteria). In total, 156 antidromic spikes were detected in 15 recordings from five mice for the scrambled RNA data set; 194 antidromic spikes detected in 15 recordings from five mice for the shRNA1 data set, and 197 antidromic spikes detected in 15 recordings from five mice for the shRNA2 data set.

2.15 | Electron microscopy of ultrathin sections

For ultrastructural visualization of myelinated axons in the white matter underlying the motor cortex, brains were fixed in a mixture of

FIGURE 4 Characterization of the effects of oligodendrocyte-specific inhibition of CGT on myelin properties. (a) Experimental protocol for AAV vector-mediated mScarlet expression in oligodendrocytes after injection into the white matter of thalamocortical motor projections. (b) Representative image of AAV vector-injected brain with mScarlet expression localized to the white matter just underneath the M1 cortex. Scale bar, 500 μm. (c) There was no difference in the density of DAPI-positive cells between the hemispheres injected or not injected with AAV. Paired *t*-test. n.s., non-significant. (d, e) Representative images (d) and quantification (e) of mScarlet expression in the white matter and co-localization with markers for oligodendrocytes (CC1), astrocytes (S100β). Scale bar in (d), 10 μm. (f) Experimental protocol for AAV vector-mediated CGT inhibition using shRNA and associated validation. (g) Representative western blots for CGT in duplicate brain samples expressing scrambled RNA, shRNA1, and shRNA2. (h) Corresponding quantitative analysis of CGT expression using western blotting. Results were normalized based on the expression level of scrambled group. One-way ANOVA followed by Tukey's test. $^{*}p < .05$, $^{**}p < .01$, n.s., non-significant. (i) Representative images of CGT and oligodendrocyte (CC1) immunostaining in brain sections from mice expressing scrambled RNA, shRNA1, and shRNA2. Scale bar, 10 μm. (j) Quantitative analysis of CGT expression in oligodendrocytes based on immunostaining data. Results were normalized based on the expression level of scrambled group. One-way ANOVA followed by Tukey's test. $^{*}p < .05$, $^{**}p < .01$, n.s., non-significant. (k) Representative images of MBP immunostaining in brain sections from mice expressing scrambled RNA, shRNA1, and shRNA2. Scale bars, left panels, 100 μm; right panels, 30 μm. (l) Quantitative analysis of relative MBP expression based on immunostaining data. Results were normalized based on the expression level of scrambled group. One-way ANOVA followed by Tukey's test. n.s., non-significant. (m) Representative electron microscopy images of white matter beneath M1 from brain sections expressing scrambled RNA, shRNA1, and shRNA2. Scale bar, 1 μm. Scatterplot of myelin thickness and axon diameter for the scrambled RNA, shRNA1, and shRNA2 groups. Color differences indicate different groups. Quantitative *g*-ratio analysis based on electron microscopy images in the scrambled RNA, shRNA1, and shRNA2 groups. One-way ANOVA followed by Tukey's test. n.s., non-significant. (n) Density of CC1-positive cells in brain sections from scrambled RNA, shRNA1, and shRNA2 expressing mice based on immunohistochemistry analysis. One-way ANOVA followed by Tukey's test. $^{*}p < .05$, $^{**}p < .01$, n.s., non-significant. (**o**) Representative images of ChR2-EYFP expression in the motor cortex (left panel; Scale bar, 200 μm) and thalamus (right panel; Scale bar, 500 μm) after injection of AAV1-Syn-ChR2-EYFP into the thalamus. ChR2 is expressed in thalamic nuclei and thalamocortical axons. (p) Schematic illustration of the experiment to antidromically activate and record thalamocortical axon spikes. (q) Representative antidromic spikes (upper panels) and raster plots (lower panels) recorded in the thalamus in mice expressing scrambled RNA (left), shRNA1 (center), and shRNA2 (right) in response to optogenetic stimulation of thalamic afferents in M1. (r) Violin plots (black lines, mean) of the latency of antidromic spike. One-way ANOVA followed by Tukey's test. $^{***}p < .001$, n.s., non-significant. Scatter plots of the latency of antidromic spikes (left panel) and the temporal dispersion of antidromic spike latencies (standard deviation [center panel] and coefficient of variation [right panel]) in recordings from mice expressing scrambled RNA, shRNA1, and shRNA2. One-way ANOVA followed by Tukey's test. $^{**}p < .01$, $^{***}p < .001$, n.s., non-significant.

10981136, 2023, 11, Downloaded from https://onlinelibrary.wiley.com/doi/10.1002/glia.24441 by Kobe University, Wiley Online Library on [14/09/2023]. See the Terms and Conditions (https://onlinelibrary.wiley.com/terms-and-conditions) on Wiley Online Library for rules of use; OA articles are governed by the applicable Creative Commons License

2% formaldehyde and 2.5% glutaraldehyde at 4°C for 8–12 h, and post-fixed with 1.5% osmium tetroxide for 1.5 h at RT. Samples were dehydrated and then embedded in epoxy resin. Ultrathin sections were observed using a JEM-1400 Flash electron microscope. Digital images were captured at ×8000 magnification using a CCD camera (Gatan, CA). Images were imported into Fiji for measuring the diameters of axons and myelin sheaths. G-ratios (axon diameter/axon plus myelin sheath diameter) were then calculated (scrambled, non-injected side: 418 axons, $n = 3$ mice; scrambled, injected side: 479 axons, $n = 3$ mice; shRNA1: 450 axons, $n = 3$ mice; shRNA2: 433 axons, $n = 3$ mice). All images were analyzed with the researcher blinded to the experimental group.

2.16 | Pharmacological CGT inhibition

To inhibit CGT during motor learning, the UGT8 Inhibitor 19 (Cayman Chemical) was orally administered at 3 mg/kg twice daily (Thurairatnam et al., 2020). After 12 days of training, six WT mice were subjected to this pharmacological CGT inhibition on days 13 to 16.

2.17 | Wire hang test

Mice used in the CGT inhibition experiments were subjected to the wire hang test for the assessment of overall muscle strength and coordination. The mice were placed on a wire suspended 35 cm above a soft fall area, and the time after which they fell was measured. Due to animal ethics considerations, this test was only conducted once.

2.18 | Statistical analysis

All data are presented as the mean ± SEM values. Statistical differences were evaluated using paired *t*-test, Wilcoxon rank sum test, analysis of variance (ANOVA) followed by Tukey's multiple comparison test, and Pearson's correlation analysis as indicated, and using MATLAB and GraphPad Prism v7.0a. *p*-values <.05 were considered statistically significant.

3 | RESULTS

3.1 | Change in task performance and neural activity during the lever-pull task

To assess the time-course of the changes in neural activity during motor learning, we first conducted *in vivo* two-photon imaging of M1 L2/3 neurons during a self-initiated lever-pull task using the right forelimb (Kato et al., 2020; Masamizu et al., 2014) (Figure 1a). In this task, mice pull the lever and hold it for 600 ms to receive a drop of water as the reward. Previous studies considered motor learning in terms of two phases—associative learning (early stage) and skill learning (late stage) (Doyon & Benali, 2005). We have also previously divided motor learning tasks into an early (days 1–4) and late (days 9–12) stage (Kato et al., 2020). To better evaluate the time course of lipid synthesis and any associated changes in neural activity, in this study, we added a middle phase (days 4–7). We divided mice into three corresponding groups (Group A: early stage, days 1–4; Group B: middle stage, days 1–7; and Group C: late stage, days 1–12) and evaluated for each group their motor task performance (number of total lever-pull trials, number of successful trials, and success rate), neural activity (two-photon Ca^{2+} imaging) and subsequent brain lipid composition (MALDI-IMS analysis) (Figure 1b–d). Across all three groups, the total number of lever-pull trials rapidly increased in the early training stage (days 1–4) and began to plateau from day 4 onwards (Figure 1b). While the number of successful trials continuously and significantly increased during each phase (Figure 1c), this was partly due to the increase in total trials. The actual success rate of lever-pull trials (successful trials/total trials) only increased during the middle and late stages (Figure 1d), consistent with previous reports (Kato et al., 2020; Masamizu et al., 2014). We also examined if neural circuitry activity changed during these phases of motor task performance using a genetically overexpressed Ca^{2+}-sensitive fluorescent protein. There were many GCaMP6f-expressing L2/3 neurons in which Ca^{2+} transients were observed, both associated with and not associated with the lever-pull movement (Figure 1e). Lever-pull-associated Ca^{2+} transients were associated with successful or unsuccessful lever-pulls, and those related to successful pulls were classified as Task-related (Figure 1e). Imaging was performed throughout the learning period (on days 2, 4, 7, and 12). To quantify any changes in neural circuitry activity, we first measured and summed the area under the curve (AUC) of each task-related Ca^{2+} transient on each image day (Figure 1e,f). We examined whether and how these task-related AUCs changed over time (day 2 vs. day 4, day 2 vs. day 7, day 2 vs. day 12), finding they increased in the middle and late stages (Figure 1g). We also assessed this change in task-related AUCs for each individual mouse (Group A: day 2 vs. day 4, Group B: day 2 vs. day 7, Group C: day 2 vs. day 12, Figure 1f) and additionally quantified for each mouse whether each neuron showed an increase in task-related AUC (a.u.) or a decrease in task-related AUC (a.u.). This enabled quantification of the proportion of increased task-related neurons in each individual mouse during the training period (Figure 1f). We could then correlate these parameters with the motor learning performances of each mouse during the different learning phases (Figure 1h,i).

In mice from Group A, the change in the number of total and successful trials correlated positively with the change in task-related AUC (a.u.) (total trials: $p = .04$, $r = .89$; successful trials: $p = .01$, $r = .96$; Figure 1h, upper and middle panels), whereas, there was no significant correlation between the success rate and task-related neural activity changes ($p = .43$, $r = .46$; Figure 1h, lower panel). There were no correlations in Group A mice between the three behavioral parameters and the change in the percentage of neurons in a mouse showing an increase in task-related activity (Figure 1l, left panels). In Group B,

10981136, 2023, 11, Downloaded from https://onlinelibrary.wiley.com/doi/10.1002/glia.24441 by Kobe University, Wiley Online Library on [14/09/2023]. See the Terms and Conditions (https://onlinelibrary.wiley.com/terms-and-conditions) on Wiley Online Library for rules of use; OA articles are governed by the applicable Creative Commons License

none of the three behavioral parameters were correlated with either the change in task-related AUC (a.u.) or the percentage of neurons with an increased task-related AUC (Figure 1h,i, center panels). For Group C, the only significant correlation was a greater increase in success rate in mice with a greater increase in the proportion of neurons showing an increase in task-related neural activity (Figure 1h,i, right panels, $p = .03$, $r = .73$). These results are consistent with a previous report (Peters et al., 2014), that showed that during the early stages of motor learning, the activity of M1 neurons associated with lever-pulling increases but is dispersed. Subsequently, in the latter stages, there is a clear population of movement-related neurons with a consistent temporal association with successful pulls. In the subsequent experiments, we assessed the correlations between these neural activity parameters (task-related AUC [a.u.] and task-related AUC [% increased neurons]) and lipid synthesis or activity-dependent myelination.

3.2 | Change in SM and GalCer levels during motor learning

To investigate whether myelin-specific lipids are correlated with the changes in the neural circuitry activity patterns associated with motor learning, we performed MALDI-IMS in brain sections of same mice we conducted lever pulling task and Ca^{2+} imaging in each group (groups A, B, and C) and quantified the levels of multiple lipids including SM, GalCer, and sulfatide. For each of these lipids, in addition to using the standard nomenclature to reflect the length of the two hydrocarbon chains, we also characterized them in terms of the ion sequestration in the MALDI samples (Table 2). Lipid signals in the left (trained) and the right (untrained) white matter beneath M1 were measured and compared. The intensities of the SM species d18:1/23:0 and d18:1/24:1 identified using M + K+ ionization were the highest in groups A and B in the trained hemisphere (Figure 2a,b,d,e). In contrast, the intensities of GalCer (d18:1/23:0) and (d18:1/24:1) were higher in the trained hemisphere in groups B and C (Figure 2a,c,d,f). These results suggest that SM is associated with the increase in task-related neural activity during the early stage of learning, while an increase in GalCer may be associated with the more coordinated neural activity during the later stage. To verify these lipid changes measured using MALDI-IMS, we also used LC–MS/MS to measure the lipids in brain samples of white matter below the M1 after 12 days of motor task training (Figure 2g). We detected multiple isomers of corresponding masses for SM (d18:1/23:0) and GalCer (d18:1/23:0 and d18:1/24:1). We only detected single isomer for SM (d18:1/24:1). The retention time for GalCer (d18:1/23:0) and GalCer

TABLE 2 Lipid species with level changes in different phases during motor learning.

Group A		Group B		Group C	
Lipid	Ion	Lipid	Ion	Lipid	Ion
SM (d18:1/23:0)	[M + K]+	SM (d18:1/22:0)	[M + K]+	GalCer (d18:1/18:0)	[M + K]+
SM (d18:1/24:1)	[M + K]+	SM (d18:1/23:0)	[M + K]+	GalCer (d18:1/23:0)	[M + K]+
SM (d18:1/25:0)	[M + K]+	SM (d18:1/24:1)	[M + K]+	GalCer (d18:1/24:0)	[M + K]+
SM (d18:1/25:0)	[M + Na]+	SM (d18:1/25:0)	[M + K]+	GalCer (d18:1/24:1)	[M + K]+
		GalCer (d18:1/18:0)	[M + K]+	GalCer (d18:1/24:0)	[M + Na]+
		GalCer (d18:1/22:0)	[M + K]+	GalCer (d18:1/24:1)	[M + Na]+
		GalCer (d18:1/23:0)	[M + K]+	Sulfatide (d18:1/16:0)	[M−H]−
		GalCer (d18:1/24:0)	[M + K]+	Sulfatide (d18:1/18:0)	[M−H]−
		GalCer (d18:1/24:1)	[M + K]+	Sulfatide (d18:1/18:1)	[M−H]−
		GalCer (d18:1/24:0)	[M + Na]+	Sulfatide (d18:1/20:0)	[M−H]−
		GalCer (d18:1/24:1)	[M + Na]+	Sulfatide (d18:1/22:0)	[M−H]−
		Sulfatide (d18:1/16:0)	[M−H]−	Sulfatide (d18:1/22:1)	[M−H]−
		Sulfatide (d18:1/18:1)	[M−H]−	Sulfatide (d18:1/24:0)	[M−H]−
		Sulfatide (d18:1/20:0)	[M−H]−	Sulfatide (d18:1/24:1)	[M−H]−
		Sulfatide (d18:1/20:1)	[M−H]−	Sulfatide (d18:1/25:0)	[M−H]−
		Sulfatide (d18:1/22:0)	[M−H]−	Sulfatide (d18:1/25:1)	[M−H]−
		Sulfatide (d18:1/22:1)	[M−H]−	Sulfatide (d18:1/26:1)	[M−H]−
		Sulfatide (d18:1/23:0)	[M−H]−		
		Sulfatide (d18:1/24:0)	[M−H]−		
		Sulfatide (d18:1/24:1)	[M−H]−		
		Sulfatide (d18:1/25:0)	[M−H]−		
		Sulfatide (d18:1/26:0)	[M−H]−		
		Sulfatide (d18:1/26:1)	[M−H]−		

10981136, 2023, 11, Downloaded from https://onlinelibrary.wiley.com/doi/10.1002/glia.24441 by Kobe University, Wiley Online Library on [14/09/2023]. See the Terms and Conditions (https://onlinelibrary.wiley.com/terms-and-conditions) on Wiley Online Library for rules of use; OA articles are governed by the applicable Creative Commons License

(d18:1/24:1) was 39.9 and 39.0 min, respectively, in all samples (10 samples) (Figure 2g). The retention time of the GalCer (d18:1/24:0) standard sample (see details in Materials and Methods) was 40.63 min, consistent with this identification of these GalCer species. In addition, we detected an *m/z* value of 264.2686 for the common main product ion spectrum peak using MS/MS both in the standard sample and in the GalCer (d18:1/23:0) and GalCer (d18:1/24: 1) samples. The composition estimate of this ion is C18H24N, which corresponds to the d18:1 component. Based on the difference between the estimated elemental composition of [M + H] + and C18H24N, it is consistent that these two identified components are GalCer (d18:1/23:0) and GalCer (d18:1/24:1), respectively. While different lipid species may have the exact same mass; however, since GalCer (d18:1/23:0) and GalCer (d18:1/24:1) have the highest notional abundance in our samples according to the LC/MS/MS results, it is further feasible that the ions corresponding to the masses of GalCer (d18:1/23:0) and GalCer (d18:1/24:1) detected using MALDI-IMS, are indeed primarily generated from GalCer (d18:1/23:0) and GalCer (d18:1/24:1) (Figure 2g). However, to provide further validation, we also performed thin-layer chromatography (TLC) of the two common biological hexosylceramides (GlcCer and GalCer) using white matter samples obtained from the mice that performed the motor learning tasks for 12 days. GalCer expression was not only higher than that of GlcCer overall, but it was significantly higher on the trained side compared to that on the untrained side. This further suggests that we have largely detected GalCer, despite having the same mass spectrum as GlcCer (Figure 2h).

3.3 | Increase in SM and GalCer levels was correlated with the neural activity of task performance

We next evaluated whether the change in lipid levels in each mouse was correlated with neural circuitry activity in individual mice by plotting the relative changes in lipid levels against the change in task-related AUC (a.u.) for each Group A mouse. There was a significant positive correlation for SM (d18:1/23:0), but no correlation with regard to GalCer in these mice (Figure 3a, left), nor any association between either lipid species with the increase in proportion of neurons increasing their activity during the initial training (task-related AUC [% increased neurons]) (Figure 3b, left). In the middle stage of learning (Group B), there were significant correlations between lipid level changes and changes in circuitry activity. Interestingly, the levels of both SM (d18:1/23:0) and GalCer (d18:1/23:0) were negatively correlated with the strength of the task-related Ca^{2+} transients and positive correlations with the change in the proportion of neurons that increased task-related activity (Figure 3a,b; middle panel). In Group C (late stage), this positive correlation between the change in GalCer (d18:1/23:0) levels and the increase in task-related populations persisted (Figure 3b, right). Together, this suggests that GalCer synthesis may facilitate the synchrony or coordination of the neural activity patterns that maintain motor learning success rates (based on the results in Figure 1), with no correlations between SM (d18:1/24:1) and GalCer (d18:1/24:1) level in this later success rates or between either lipid and increased overall task-related activity (Figure S1 and Table 2). These results strengthen the notion that SM synthesis contributes to the increased activity of task-related neurons during the early stage of learning and that GalCer synthesis is associated with neural circuitry tuning in the middle and late stages of motor learning.

3.4 | Inhibition of GalCer synthesis reduced task performance

As GalCer is synthesized from SM by the enzyme CGT in oligodendrocytes, we further tested whether GalCer contributes to motor learning and neural synchrony by targeting inhibition of CGT using AAV-mediated, oligodendrocyte-specific shRNA expression. We first examined correct targeting of the AAV-mediated shRNA expression in the motor pathway of thalamocortical projections using our injection approach and the MAG promoter. We first evaluated the general impact of our AAV vector injection on cell viability by staining for DAPI, and found no significant difference in the number of DAPI-positive cells between the injected and non-injected sides (Figure 4a–c). Next, we coupled our MAG promoter with AAV coding for mScarlet and immune-stained for cell subtype markers of oligodendrocytes, astrocytes, and neurons (Figure 4a–d). Low-magnification images of brain sections revealed localized expression in the white matter of the thalamocortical motor pathway (Figure 4a,b) with higher magnification images (Figure 4d,e) showing most (85.6 ± 0.013%) mScarlet-positive cells also stained positive for the oligodendrocyte marker CC1, while some (14.2 ± 0.012%) were positive for both CC1- and the astrocyte marker S100β. Almost no S100β only -positive cells nor NeuN-positive cells were detected co-labeled with mScarlet (Figure 4d,e), suggesting AAV expression is mostly restricted to oligodendrocyte-lineage cells. We next validated that the shRNA could reduce CGT expression *in vitro* using CMT 167 cells (Figure S2a) and *in vivo* via AAV-mediated inhibition (Figure 4f–j). We quantified CGT level after shRNA expression using western blotting (Figure 4f–h) and immunostaining (Figure 4f,i,j), utilizing two different shRNAs (shRNA1, shRNA2). CGT expression was significantly lower in the MAG-shRNA groups (with both shRNA1 and shRNA2) compared to that in the MAG-scrambled group (Figure 4f–j). To probe what aspects of myelin beyond GalCer lipid synthesis may be impacted by CGT inhibition, we used a number of biochemical, histological, and functional measures. Initially, we immune-stained for MBP (a key component of myelin ensheathment to axons) and directly measured myelin thickness. MBP expression intensity was not different between non-injected and scrambled AAV injected hemispheres (Figure S2b) and similarly 2 to 3 weeks of shRNA expression did not affect relative MBP expression compared with that seen with scrambled shRNA expression (Figure 4k,l). Using electron microscopy, we measured axon and myelin thickness and quantified the ratio of myelin and axon diameters (the *g*-ratio). This *g*-ratio was not different in sub-cortical white matter in thin brain sections from mice expressing scrambled shRNA (both the non-AAV and AAV side), shRNA1, or

10981136, 2023, 11, Downloaded from https://onlinelibrary.wiley.com/doi/10.1002/glia.24441 by Kobe University, Wiley Online Library on [14/09/2023]. See the Terms and Conditions (https://onlinelibrary.wiley.com/terms-and-conditions) on Wiley Online Library for rules of use; OA articles are governed by the applicable Creative Commons License

shRNA2 (Figures 4m and S2c). Furthermore, the correlation between myelin thickness and axon diameter were similar in each experimental group (Figures 4m and S2c). We did detect a decrease in the density of CC1-positive oligodendrocytes in sections from mice expressing shRNAs, suggesting that CGT expression or GalCer levels may contribute to oligodendrocyte differentiation (Figure 4n). We also used two functional assays, firstly measuring latency and dispersion of action potential propagation along cortico-thalamic tracts

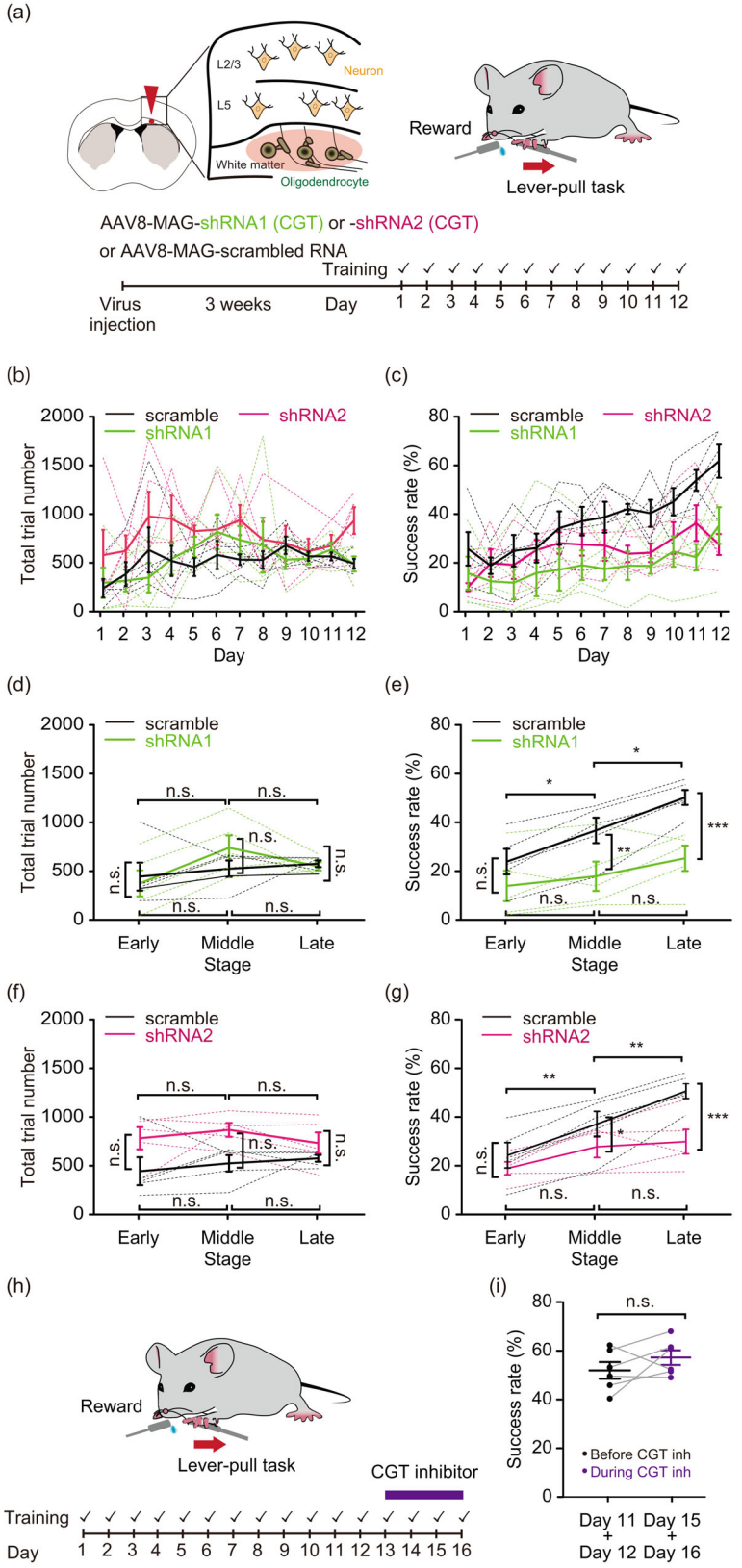

FIGURE 5 Deficits in motor learning after inhibition of GalCer synthesis. (a) Experimental protocol of oligodendrocyte-specific CGT inhibition using shRNAs to inhibit GalCer expression during motor learning. AAV8-MAG-shRNAs or scrambled RNA solution was injected into the white matter underlying the M1. (b, c) Plot of the total number of lever-pull trials (b) or success rate (c) over 12 days motor training in control (scrambled RNA, black) and CGT inhibited (shRNA1, green; shRNA2, red) mice. (d, e) Total number of lever-pull trials (d) or success rate (e) grouped across the early stage of learning (days 1–4), the middle stage (days 5–7), and the late stage (days 9–12). Five scrambled RNA AAV vector-injected mice (black) and five shRNA1 AAV vector-injected mice (green) were used. Two-way ANOVA followed by Tukey's test. Data are presented as the mean ± SEM values. n.s., non-significant, *$p < .05$, **$p < .01$, ***$p < .001$ (d) Total number of trials: scrambled vs. shRNA1, $F_{1,24} = 0.10$, $p = .99$ (early), $p = .77$ (middle), $p = 1.0$ (late); scrambled, $F_{2,24} = 4.40$, $p = .98$ (early vs. middle), $p = 1.0$ (middle vs. late); shRNA1, $F_{2,24} = 4.40$, $p = .091$ (early vs. middle), $p = .59$ (middle vs. late); (e) Success rate: scrambled vs. shRNA1, $F_{1,24} = 5.64$, $p = .0590$ (early), $p = .0015$ (middle), $p = 2.0 \times 10^{-4}$ (late); scrambled, $F_{2,24} = 22.13$, $p = .016$ (early vs. middle), $p = .012$ (middle vs. late); shRNA1, $F_{2,24} = 22.13$, $p = .73$ (early vs. middle), $p = .20$ (middle vs. late). (f, g) Total number of lever-pull trials (f) or success rate (g) grouped across the early stage of learning (days 1–4), the middle stage (days 5–7), and the late stage (days 9–12). Five scrambled RNA AAV vector-injected mice (black) and five shRNA2 AAV vector-injected mice (red) were used. Two-way ANOVA followed by Tukey's test. Data are presented as the mean ± SEM values. n.s., non-significant, *$p < .05$, **$p < .01$, ***$p < .001$. (f): Total number of trials: scrambled vs. shRNA2, $F_{1,24} = 43.62$, $p = .22$ (early), $p = .21$ (middle), $p = .84$ (late); scrambled, $F_{2,24} = 0.59$, $p = .99$ (early vs. middle), $p = 1.0$ (middle vs. late); shRNA2, $F_{2,24} = 0.59$, $p = .98$ (early vs. middle), $p = .90$ (middle vs. late) (g) Success rate: scrambled vs. shRNA2, $F_{1,24} = 7.79$, $p = .33$ (early), $p = .040$ (middle), $p = 3.0 \times 10^{-4}$ (late); scrambled, $F_{2,24} = 29.56$, $p = .0066$ (early vs. middle), $p = .0046$ (middle vs. late); shRNA2, $F_{2,24} = 29.56$, $p = .050$ (early vs. middle), $p = .94$ (middle vs. late). (h) Experimental scheme for pharmacological CGT inhibition in mice with established motor learning. (i) Success rates across days 11 + 12 (control) was not different from that across days 15 + 16 (with CGT inhibition). Success rate data are presented as the mean ± SEM values. Paired *t*-test. n.s., non-significant.

10981136, 2023, 11, Downloaded from https://onlinelibrary.wiley.com/doi/10.1002/glia.24441 by Kobe University, Wiley Online Library on [14/09/2023]. See the Terms and Conditions (https://onlinelibrary.wiley.com/terms-and-conditions) on Wiley Online Library for rules of use; OA articles are governed by the applicable Creative Commons License

(Figure 4o–r). In mice expressing either the scrambled RNA or shRNA in oligodendrocytes within thalamocortical white matter projection populations, we co-expressed ChR2 (synapsin promoter) in thalamic nuclei including those with motor cortex projections (Figure 4o). Sixteen-channel electrode arrays were inserted into the thalamus, and a fiber-optic cable placed close to the exposed cortex to antidromically activate thalamocortical motor projections (Figure 4p). There was no change in the latency of the largest and fastest antidromic spikes at the individual mouse level, suggesting no major myelin deficit to affect on conduction velocity (Figure 4q,r). When multiple spikes were simultaneously recorded across the electrode array, the temporal dispersion of latencies of these spikes increased significantly after CGT inhibition (Figure 4q,r), reflecting that a small but significant change of the individual antidromic spike latency in the MAG-shRNA group compared to that in the scrambled group (Figure 4r). This suggests a subtle functional impairment in conduction in some axons due to reduced oligodendrocyte CGT expression—possibly those of slower latency or with thinner sheaths have slightly impaired conduction, or CGT activity is non-homogenous across oligodendrocytes. We further assessed the impact of reduced CGT expression on motor function using a wire hang test. The time that it took for mice to let go of the wire did not differ between groups expressing scrambled RNA, shRNA1, or shRNA2, suggesting no broad deficits of motor strength or fatigue (Figure S2d). Having thoroughly validated the approach to reduce CGT expression *in vivo* and evaluated its consequences on myelin structure and function, we subjected the different mice groups to the motor learning paradigm (Figure 5a–g). The total number of lever-pull trials in the early stage did not differ between the scrambled RNA- and the shRNA1- or shRNA2-injected mice, again suggesting no broad deficits in motor function (Figure 5b,d,f). However, knockdown of CGT decreased the rate of successful learned association between lever-pull and water reward during both the middle and late stages of learning (Figure 5c,e,g). This is consistent with the wider temporal dispersion of axonal conduction in the MAG-shRNA group (Figure 4q,r) which we propose is required to synchronize neural circuitry required for learning. Additionally, we did not find any correlation between either the total number of lever-pulls and the success rate, nor the latency to fall in the wire hang test and the success rate, suggesting that successful learning was not related to basic motor function (Figure S2e). Furthermore, reduced CGT expression was associated with lower expression levels of MBP mRNA induced by motor learning, suggesting the potential reduction of oligodendrocyte differentiation (Figure S2f).

Finally, to test whether CGT inhibition more specifically impaired some aspect of lever-pulling behavior, we extended an additional 4 days of lever-pull testing (days 13–16) in mice with established motor learning while inhibiting CGT. To this end, we pharmacologically inhibited CGT through twice daily administration of the CGT blocker UGT8 Inhibitor 19 (oral, 3 mg/kg; [Thurairatnam et al., 2020]). The mean success rate on day 11 + day 12 and on day 15 + day 16 remained unchanged in these CGT-treated mice, indicating that CGT inhibition affected motor learning rather than lever-pulling behavior and that did not affect on the mice established motor learning (Figure 5h,i).

4 | DISCUSSION

This study suggests that SM and GalCer levels change during the different stages of motor learning and these changes are associated with the learning-induced patterns of neural activity. SM levels were specifically higher in the early stage of learning, while GalCer levels appear to increase in the middle- and late-stages of learning. Strikingly, the specific inhibition of GalCer synthesis in oligodendrocytes associated with thalamocortical motor projections impaired these latter aspects of motor learning, perhaps through subtle changes in axonal conduction to effect neural circuitry synchrony. This suggests synthesis of GalCer helps stabilize circuitry involved in motor learning and adds a new aspect to adaptive myelination—the activity-dependent myelination required for motor learning.

The myelin that comprises white matter is mainly composed of lipids but these are closely associated with specific myelin proteins. White matter adaptive plasticity in response to learning and training is correlated with the levels of several myelin-related lipids and proteins. Interactions between sphingolipids and the myelin-related proteins such as MBP and PLP1 is involved in white matter plasticity and activity-dependent myelination (Ozgen et al., 2016; Wattenberg, 2019). During development, oligodendrocytes produce GalCer and sulfatide prior to the increase in expression of MBP and PLP1, indicating a specific timing sequence in myelin formation (Ozgen et al., 2016). In addition, sphingolipids actively regulate myelin-related proteins by organizing into specialized structures such as lipid rafts to support the dynamics relevant to myelin function (Gielen et al., 2006; Ozgen et al., 2016). Consistently, our results showed that SM levels increased in the early stage of motor learning when the number of successful and total lever-pulls was increasing, and the neural activity patterns associated with successful trials were broadly increasing (Figures 1, 2, and 3). GalCer synthesis increased from the middle stage of motor learning and persisted to the late stage, correlating to the time when success rate was increasing independent of total trials (Figures 1, 2, and 3). During these latter periods, neural circuitry associated with successful lever-pulls are being consolidated and this is likely to involve greater synchrony of individual neurons in these circuitry. Previous studies have also implicated interactions between these sphingolipids and proteins as crucial for the formation and maintenance of myelin, and in the regulation of protein transport and molecular organization within the myelin sheath (Aggarwal et al., 2011; Ozgen et al., 2016). Consistently, genetic deletion of CGT results in deficient GalCer synthesis, reduced MBP expression, unstable and thin myelin sheaths, progressive demyelination, and deficits in motor function, and these symptoms are completely ameliorated by oligodendrocyte-specific CGT re-expression (Zöller et al., 2005). Taken together, these findings support our observations that SM and GalCer production is correlated with establishing neural activity patterns and synchrony required for the motor learning process. The major lipids in the myelin of oligodendrocyte and white matter, including SM, GalCer, and sulfatides, have very long saturated fatty acyl chains (C22–24) (Yurlova et al., 2011), and SM (C24) (Don et al., 2014; Sugimoto et al., 2015) and GalCer (C24) (Don et al., 2014; O'Brien et al., 1964; Ozgen et al., 2016). While we detected that changes in levels of both SM (C23, C24) and GalCer (C23, C24) species correlated with improvement of motor behavior performance; interestingly, only changes

10981136, 2023, 11, Downloaded from https://onlinelibrary.wiley.com/doi/10.1002/glia.24441 by Kobe University, Wiley Online Library on [14/09/2023]. See the Terms and Conditions (https://onlinelibrary.wiley.com/terms-and-conditions) on Wiley Online Library for rules of use; OA articles are governed by the applicable Creative Commons License

in the levels of the shorter species, SM (C23) and GalCer (C23), were positively correlated with the neural activity synchronization associated motor learning (Figure 3). This may be because the longer SM (C24) and GalCer (C24) species are more abundant in the white matter (Don et al., 2014; Ozgen et al., 2016), and the changes due to motor learning for these longer species were small (Figure S1).

Activity-dependent proliferation and differentiation of oligodendrocyte precursor cells and myelination contribute significantly to learning (McKenzie et al., 2014; Pan et al., 2020; Steadman et al., 2020; Xiao et al., 2016; Xin & Chan, 2020). Deletion of the gene encoding MyRF, a transcription factor that oligodendrocytes need to initiate and maintain myelination, inhibits oligodendrocyte precursor cell differentiation, thereby inhibiting myelination, consequently leading to deficits in motor learning (McKenzie et al., 2014; Xiao et al., 2016) and consolidation of fear memory (Pan et al., 2020) and spatial memory (Steadman et al., 2020). Activity-dependent myelination also affecting neural activity patterns (Kato et al., 2020). Using *in vivo* Ca^{2+} imaging with fiber photometry, neural activity in the medial prefrontal cortex in MyRF-deleted mice was impaired during the consolidation of remote fear memory and was rescued by the administration of clemastine, which induces the formation of new myelin (Pan et al., 2020). Transgenic PLP1-overexpressing mice show a reduced conduction velocity due to subtle abnormalities in myelin structure (Tanaka et al., 2006; Tanaka et al., 2009) and in disruption of activity-dependent myelination (Kato et al., 2020). Furthermore, these mice also show motor learning impairment, which is inversely correlated with an increased spontaneous activity in the motor cortex. A temporal dispersion of axonal conduction is also observed in the thalamocortical axons of these mice, and restoring partially the synchrony of thalamocortical inputs by the repetitive pairing of forelimb movements with optogenetic stimulation of these axon terminals, also partially restores the motor learning deficit (Kato et al., 2020). These findings suggested that precise control of myelination helps to maintain the synchronous arrival of spikes over long-range axons and facilitates the tightly timed neural circuit activity required for motor learning. Our current results indicate that one aspect of this activity-dependent myelination involves new lipid synthesis, and this may support the requisite increase synchronicity by enhancing conduction velocity of some axons within the motor learning circuitry. While changes in hippocampal lipid synthesis have been observed during the extinction of food-rewarded behavior (Huston et al., 2016), we believe this is the first report to directly measure and correlate lipid synthesis in white matter during motor learning and to correlate these changes to both behavioral improvements and neural circuitry changes.

The abnormal metabolism of sphingolipids (Hussain et al., 2019; Trayssac et al., 2018) and prototypical myelin lipids (including GalCer and sulfatides) (Couttas et al., 2016) has been associated with neurodegenerative diseases such as Alzheimer's disease. Moreover, dysfunction of white matter is observed in older individuals and patients with neurodegenerative disorders (Amlien & Fjell, 2014; Back et al., 2011; Bennett & Madden, 2014; Lee et al., 2016). Altered synthesis and metabolism of myelin lipids (El-Sitt et al., 2019) may contribute to the progression of such neurodegenerative disorders.

Our study indicates that lipid levels change at distinct times during motor learning and these changes are correlated with the changes in neural circuitry activity that underlie motor learning. Furthermore, by disrupting oligodendrocyte lipid synthesis, we could demonstrate a causal relationship between GalCer synthesis and the latter stages of motor learning, which we propose is due to the requirement of GalCer to help synchronize neural circuitry activity associated with motor learning patterns. Further investigation into how specific myelin lipids are regulated and change during learning and in neurodegenerative diseases could provide novel therapeutic strategies for diseases involving impaired white matter function.

AUTHOR CONTRIBUTIONS

Daisuke Kato, Mitsutoshi Setou, and Hiroaki Wake designed the study. Daisuke Kato, Yuki Aoyama, Kazuki Nishida, Yutaka Takahashi, Takumi Sakamoto, Ikuko Takeda, Tsuyako Tatematsu, Shiori Go, Yutaro Saito, Shiho Kunishima, Jinlei Cheng, and Lingnan Hou performed the experiments based on advice from Yoshihisa Tachibana, Shouta Sugio, Reon Kondo, Fumihiro Eto, Shumpei Sato, Andrew J. Moorhouse, Ikuko Yao, Kenji Kadomatsu, and Mitsutoshi Setou. Daisuke Kato, Yuki Aoyama, Kazuki Nishida, Yutaka Takahashi, and Hiroaki Wake analyzed the data. Daisuke Kato, Andrew J. Moorhouse, and Hiroaki Wake wrote the manuscript with inputs from all other authors.

ACKNOWLEDGMENTS

We thank Douglas Kim (GINIE Project, Janelia Farm Research Campus [HHMI]) for providing the AAV1-hSyn-GCaMP6f-WPRE-SV40 construct and Karl Deisseroth (Stanford University) for providing the AAV1-Syn-ChR2 (H134R)-EYFP construct. We also thank Division for Medical Research Engineering, Nagoya University Graduate School of Medicine for analysis with IMARIS. This work was supported by the FOREST program (grant number JPMJFR2145 to Daisuke Kato); Grants-in-Aid for Young Scientists (grant number 20K16574 to Daisuke Kato); Nagoya University CIBoG WISE program from MEXT (to Yuki Aoyama); Grants-in-Aid for Scientific Research on Innovative Areas (grant numbers 19H04753, 19H05219, and 25110732 to Hiroaki Wake); Grants-in-Aid for Transformative Research Areas (A) (grant number 20H05699 to Hiroaki Wake and 21H05587 to Daisuke Kato); Fostering Joint International Research (B) (grant number 20KK0170 to Hiroaki Wake); Grants-in-Aid for Scientific Research (B) (grant numbers 18H02598 and 21H02662 to Hiroaki Wake); Grants-in-Aid for Young Scientists (A) (grant number 26710004 to Hiroaki Wake); the Japan Agency for Medical Research and Development (grant number JP22ak0101150 to Daisuke Kato and JP23gm1410011 h0002 to Kenji Kadomatsu and Hiroaki Wake); and JST CREST (grant numbers JPMJCR1755 and JPMJCR22P6 to Hiroaki Wake).

CONFLICT OF INTEREST STATEMENT

The authors have no financial conflicts of interest.

DATA AVAILABILITY STATEMENT

Most of the data that support the findings of this study (except for MALDI-IMS and Ca^{2+} data) are available in the supplementary material of this article. MALDI-IMS and Ca^{2+} data are available from the corresponding author upon reasonable request.

10981136, 2023, 11, Downloaded from https://onlinelibrary.wiley.com/doi/10.1002/glia.24441 by Kobe University, Wiley Online Library on [14/09/2023]. See the Terms and Conditions (https://onlinelibrary.wiley.com/terms-and-conditions) on Wiley Online Library for rules of use; OA articles are governed by the applicable Creative Commons License

ORCID

Andrew J. Moorhouse https://orcid.org/0000-0001-7957-2498
Hiroaki Wake https://orcid.org/0000-0002-8543-4590

REFERENCES

Aggarwal, S., Yurlova, L., & Simons, M. (2011). Central nervous system myelin: Structure, synthesis and assembly. *Trends in Cell Biology*, *21*(10), 585–593. https://doi.org/10.1016/j.tcb.2011.06.004

Amlien, I. K., & Fjell, A. M. (2014). Diffusion tensor imaging of white matter degeneration in Alzheimer's disease and mild cognitive impairment. *Neuroscience*, *276*, 206–215. https://doi.org/10.1016/j.neuroscience.2014.02.017

Back, S. A., Kroenke, C. D., Sherman, L. S., Lawrence, G., Gong, X., Taber, E. N., Sonnen, J. A., Larson, E. B., & Montine, T. J. (2011). White matter lesions defined by diffusion tensor imaging in older adults. *Annals of Neurology*, *70*(3), 465–476. https://doi.org/10.1002/ana.22484

Bennett, I. J., & Madden, D. J. (2014). Disconnected aging: Cerebral white matter integrity and age-related differences in cognition. *Neuroscience*, *276*, 187–205. https://doi.org/10.1016/j.neuroscience.2013.11.026

Bosio, A., Binczek, E., Haupt, W. F., & Stoffel, W. (1998). Composition and biophysical properties of myelin lipid define the neurological defects in galactocerebroside- and sulfatide-deficient mice. *Journal of Neurochemistry*, *70*(1), 308–315. https://doi.org/10.1046/j.1471-4159.1998.70010308.x

Chen, M. B., Jiang, X., Quake, S. R., & Südhof, T. C. (2020). Persistent transcriptional programmes are associated with remote memory. *Nature*, *587*(7834), 437–442. https://doi.org/10.1038/s41586-020-2905-5

Ciocchi, S., Passecker, J., Malagon-Vina, H., Mikus, N., & Klausberger, T. (2015). Brain computation. Selective information routing by ventral hippocampal CA1 projection neurons. *Science*, *348*(6234), 560–563. https://doi.org/10.1126/science.aaa3245

Corrigan, N. M., Yarnykh, V. L., Hippe, D. S., Owen, J. P., Huber, E., Zhao, T. C., & Kuhl, P. K. (2021). Myelin development in cerebral gray and white matter during adolescence and late childhood. *NeuroImage*, *227*, 117678. https://doi.org/10.1016/j.neuroimage.2020.117678

Couttas, T. A., Kain, N., Suchowerska, A. K., Quek, L. E., Turner, N., Fath, T., Garner, B., & Don, A. S. (2016). Loss of ceramide synthase 2 activity, necessary for myelin biosynthesis, precedes tau pathology in the cortical pathogenesis of Alzheimer's disease. *Neurobiology of Aging*, *43*, 89–100. https://doi.org/10.1016/j.neurobiolaging.2016.03.027

Dadar, M., Mahmoud, S., Zhernovaia, M., Camicioli, R., Maranzano, J., & Duchesne, S. (2022). White matter hyperintensity distribution differences in aging and neurodegenerative disease cohorts. *NeuroImage: Clinical*, *36*, 103204. https://doi.org/10.1016/j.nicl.2022.103204

de Faria, O., Jr., Pivonkova, H., Varga, B., Timmler, S., Evans, K. A., & Káradóttir, R. T. (2021). Periods of synchronized myelin changes shape brain function and plasticity. *Nature Neuroscience*, *24*(11), 1508–1521. https://doi.org/10.1038/s41593-021-00917-2

Don, A. S., Hsiao, J. H., Bleasel, J. M., Couttas, T. A., Halliday, G. M., & Kim, W. S. (2014). Altered lipid levels provide evidence for myelin dysfunction in multiple system atrophy. *Acta Neuropathologica Communications*, *2*, 150. https://doi.org/10.1186/s40478-014-0150-6

Doyon, J., & Benali, H. (2005). Reorganization and plasticity in the adult brain during learning of motor skills. *Current Opinion in Neurobiology*, *15*(2), 161–167. https://doi.org/10.1016/j.conb.2005.03.004

el-Sitt, S., Soueid, J., Maalouf, K., Makhoul, N., al Ali, J., Makoukji, J., Asser, B., Daou, D., Harati, H., & Boustany, R. M. (2019). Exogenous Galactosylceramide as potential treatment for CLN3 disease. *Annals of Neurology*, *86*(5), 729–742. https://doi.org/10.1002/ana.25573

Fields, R. D. (2015). A new mechanism of nervous system plasticity: Activity-dependent myelination. *Nature Reviews. Neuroscience*, *16*(12), 756–767. https://doi.org/10.1038/nrn4023

Fields, R. D., & Bukalo, O. (2020). Myelin makes memories. *Nature Neuroscience*, *23*(4), 469–470. https://doi.org/10.1038/s41593-020-0606-x

Gibson, E. M., Purger, D., Mount, C. W., Goldstein, A. K., Lin, G. L., Wood, L. S., Inema, I., Miller, S. E., Bieri, G., Zuchero, J. B., Barres, B. A., Woo, P. J., Vogel, H., & Monje, M. (2014). Neuronal activity promotes oligodendrogenesis and adaptive myelination in the mammalian brain. *Science*, *344*(6183), 1252304. https://doi.org/10.1126/science.1252304

Gielen, E., Baron, W., Vandeven, M., Steels, P., Hoekstra, D., & Ameloot, M. (2006). Rafts in oligodendrocytes: Evidence and structure-function relationship. *Glia*, *54*(6), 499–512. https://doi.org/10.1002/glia.20406

Go, S., Go, S., Veillon, L., Ciampa, M. G., Mauri, L., Sato, C., Kitajima, K., Prinetti, A., Sonnino, S., & Inokuchi, J. I. (2017). Altered expression of ganglioside GM3 molecular species and a potential regulatory role during myoblast differentiation. *The Journal of Biological Chemistry*, *292*(17), 7040–7051. https://doi.org/10.1074/jbc.M116.771253

Gupta, V., Patwardhan, G. A., Zhang, Q. J., Cabot, M. C., Jazwinski, S. M., & Liu, Y. Y. (2010). Direct quantitative determination of ceramide glycosylation in vivo: A new approach to evaluate cellular enzyme activity of glucosylceramide synthase. *Journal of Lipid Research*, *51*(4), 866–874. https://doi.org/10.1194/jlr.D002949

Hakak, Y., Walker, J. R., Li, C., Wong, W. H., Davis, K. L., Buxbaum, J. D., Haroutunian, V., & Fienberg, A. A. (2001). Genome-wide expression analysis reveals dysregulation of myelination-related genes in chronic schizophrenia. *Proceedings of the National Academy of Sciences of the United States of America*, *98*(8), 4746–4751. https://doi.org/10.1073/pnas.081071198

Hussain, G., Wang, J., Rasul, A., Anwar, H., Imran, A., Qasim, M., Zafar, S., Kamran, S. K. S., Razzaq, A., Aziz, N., Ahmad, W., Shabbir, A., Iqbal, J., Baig, S. M., & Sun, T. (2019). Role of cholesterol and sphingolipids in brain development and neurological diseases. *Lipids in Health and Disease*, *18*(1), 26. https://doi.org/10.1186/s12944-019-0965-z

Huston, J. P., Kornhuber, J., Mühle, C., Japtok, L., Komorowski, M., Mattern, C., Reichel, M., Gulbins, E., Kleuser, B., Topic, B., de Souza Silva, M. A., & Müller, C. P. (2016). A sphingolipid mechanism for behavioral extinction. *Journal of Neurochemistry*, *137*(4), 589–603. https://doi.org/10.1111/jnc.13537

Kato, D., & Wake, H. (2019). Activity-dependent myelination. *Advances in Experimental Medicine and Biology*, *1190*, 43–51. https://doi.org/10.1007/978-981-32-9636-7_4

Kato, D., Wake, H., Lee, P. R., Tachibana, Y., Ono, R., Sugio, S., Tsuji, Y., Tanaka, Y. H., Tanaka, Y. R., Masamizu, Y., Hira, R., Moorhouse, A. J., Tamamaki, N., Ikenaka, K., Matsukawa, N., Fields, R. D., Nabekura, J., & Matsuzaki, M. (2020). Motor learning requires myelination to reduce asynchrony and spontaneity in neural activity. *Glia*, *68*(1), 193–210. https://doi.org/10.1002/glia.23713

Kister, A., & Kister, I. (2022). Overview of myelin, major myelin lipids, and myelin-associated proteins. *Frontiers in Chemistry*, *10*, 1041961. https://doi.org/10.3389/fchem.2022.1041961

Lee, S., Viqar, F., Zimmerman, M. E., Narkhede, A., Tosto, G., Benzinger, T. L., Marcus, D. S., Fagan, A. M., Goate, A., Fox, N. C., Cairns, N. J., Holtzman, D. M., Buckles, V., Ghetti, B., McDade, E., Martins, R. N., Saykin, A. J., Masters, C. L., Ringman, J. M., … for the Dominantly Inherited Alzheimer Network. (2016). White matter hyperintensities are a core feature of Alzheimer's disease: Evidence from the dominantly inherited Alzheimer network. *Annals of Neurology*, *79*(6), 929–939. https://doi.org/10.1002/ana.24647

Maganti, R. J., Hronowski, X. L., Dunstan, R. W., Wipke, B. T., Zhang, X., Jandreski, L., Hamann, S., & Juhasz, P. (2019). Defining changes in the spatial distribution and composition of brain lipids in the shiverer and cuprizone mouse models of myelin disease. *The Journal of Histochemistry and Cytochemistry*, *67*(3), 203–219. https://doi.org/10.1369/0022155418815860

Masamizu, Y., Tanaka, Y. R., Tanaka, Y. H., Hira, R., Ohkubo, F., Kitamura, K., Isomura, Y., Okada, T., & Matsuzaki, M. (2014). Two distinct layer-specific dynamics of cortical ensembles during learning of a motor task. *Nature Neuroscience*, *17*(7), 987–994. https://doi.org/10.1038/nn.3739

McKenzie, I. A., Ohayon, D., Li, H., Paes de Faria, J., Emery, B., Tohyama, K., & Richardson, W. D. (2014). Motor skill learning requires

10981136, 2023, 11, Downloaded from https://onlinelibrary.wiley.com/doi/10.1002/glia.24441 by Kobe University, Wiley Online Library on [14/09/2023]. See the Terms and Conditions (https://onlinelibrary.wiley.com/terms-and-conditions) on Wiley Online Library for rules of use; OA articles are governed by the applicable Creative Commons License

active central myelination. *Science*, *346*(6207), 318–322. https://doi.org/10.1126/science.1254960

Nave, K. A. (2010). Myelination and support of axonal integrity by glia. *Nature*, *468*(7321), 244–252. https://doi.org/10.1038/nature09614

O'Brien, J. S., Fillerup, D. L., & Mead, J. F. (1964). Brain lipids: I. Quantification and fatty acid composition of cerebroside sulfate in human cerebral gray and white matter. *Journal of Lipid Research*, *5*, 109–116.

Ozgen, H., Baron, W., Hoekstra, D., & Kahya, N. (2016). Oligodendroglial membrane dynamics in relation to myelin biogenesis. *Cellular and Molecular Life Sciences*, *73*(17), 3291–3310. https://doi.org/10.1007/s00018-016-2228-8

Pan, S., Mayoral, S. R., Choi, H. S., Chan, J. R., & Kheirbek, M. A. (2020). Preservation of a remote fear memory requires new myelin formation. *Nature Neuroscience*, *23*(4), 487–499. https://doi.org/10.1038/s41593-019-0582-1

Peters, A. J., Chen, S. X., & Komiyama, T. (2014). Emergence of reproducible spatiotemporal activity during motor learning. *Nature*, *510*(7504), 263–267. https://doi.org/10.1038/nature13235

Sampaio-Baptista, C., & Johansen-Berg, H. (2017). White matter plasticity in the adult brain. *Neuron*, *96*(6), 1239–1251. https://doi.org/10.1016/j.neuron.2017.11.026

Sampaio-Baptista, C., Khrapitchev, A. A., Foxley, S., Schlagheck, T., Scholz, J., Jbabdi, S., DeLuca, G. C., Miller, K. L., Taylor, A., Thomas, N., Kleim, J., Sibson, N. R., Bannerman, D., & Johansen-Berg, H. (2013). Motor skill learning induces changes in white matter microstructure and myelination. *The Journal of Neuroscience*, *33*(50), 19499–19503. https://doi.org/10.1523/jneurosci.3048-13.2013

Scholz, J., Klein, M. C., Behrens, T. E., & Johansen-Berg, H. (2009). Training induces changes in white-matter architecture. *Nature Neuroscience*, *12*(11), 1370–1371. https://doi.org/10.1038/nn.2412

Steadman, P. E., Xia, F., Ahmed, M., Mocle, A. J., Penning, A. R. A., Geraghty, A. C., Steenland, H. W., Monje, M., Josselyn, S. A., & Frankland, P. W. (2020). Disruption of Oligodendrogenesis impairs memory consolidation in adult mice. *Neuron*, *105*(1), 150–164.e156. https://doi.org/10.1016/j.neuron.2019.10.013

Sugimoto, M., Shimizu, Y., Yoshioka, T., Wakabayashi, M., Tanaka, Y., Higashino, K., Numata, Y., Sakai, S., Kihara, A., Igarashi, Y., & Kuge, Y. (2015). Histological analyses by matrix-assisted laser desorption/ionization-imaging mass spectrometry reveal differential localization of sphingomyelin molecular species regulated by particular ceramide synthase in mouse brains. *Biochimica et Biophysica Acta*, *1851*(12), 1554–1565. https://doi.org/10.1016/j.bbalip.2015.09.004

Sun, Y., Blanco-Centurion, C., Bendell, E., Vidal-Ortiz, A., Luo, S., & Liu, M. (2019). Activity dynamics of amygdala GABAergic neurons during cataplexy of narcolepsy. *eLife*, *8*, e48311. https://doi.org/10.7554/eLife.48311

Takanashi, Y., Funai, K., Sato, S., Kawase, A., Tao, H., Takahashi, Y., Shiiya, N., Setou, M., Kahyo, T., & Shiiya, N. (2020). Sphingomyelin (d35:1) as a novel predictor for lung adenocarcinoma recurrence after a radical surgery: A case-control study. *BMC Cancer*, *20*(1), 800. https://doi.org/10.1186/s12885-020-07306-1

Tanaka, H., Ikenaka, K., & Isa, T. (2006). Electrophysiological abnormalities precede apparent histological demyelination in the central nervous system of mice overexpressing proteolipid protein. *Journal of Neuroscience Research*, *84*(6), 1206–1216. https://doi.org/10.1002/jnr.21018

Tanaka, H., Ma, J., Tanaka, K. F., Takao, K., Komada, M., Tanda, K., Suzuki, A., Ishibashi, T., Baba, H., Isa, T., Shigemoto, R., Ono, K., Miyakawa, T., & Ikenaka, K. (2009). Mice with altered myelin proteolipid protein gene expression display cognitive deficits accompanied by abnormal neuron-glia interactions and decreased conduction velocities. *The Journal of Neuroscience*, *29*(26), 8363–8371. https://doi.org/10.1523/jneurosci.3216-08.2009

Thévenaz, P., Ruttimann, U. E., & Unser, M. (1998). A pyramid approach to subpixel registration based on intensity. *IEEE Transactions on Image Processing*, *7*(1), 27–41. https://doi.org/10.1109/83.650848

Thurairatnam, S., Lim, S., Barker, R. H., Jr., Choi-Sledeski, Y. M., Hirth, B. H., Jiang, J., Macor, J. E., Makino, E., Maniar, S., Musick, K., Pribish, J. R., & Munson, M. (2020). Brain penetrable inhibitors of ceramide galactosyltransferase for the treatment of lysosomal storage disorders. *ACS Medicinal Chemistry Letters*, *11*(10), 2010–2016. https://doi.org/10.1021/acsmedchemlett.0c00120

Tian, L., Hires, S. A., Mao, T., Huber, D., Chiappe, M. E., Chalasani, S. H., Petreanu, L., Akerboom, J., McKinney, S. A., Schreiter, E. R., Bargmann, C. I., Jayaraman, V., Svoboda, K., & Looger, L. L. (2009). Imaging neural activity in worms, flies and mice with improved GCaMP calcium indicators. *Nature Methods*, *6*(12), 875–881. https://doi.org/10.1038/nmeth.1398

Trayssac, M., Hannun, Y. A., & Obeid, L. M. (2018). Role of sphingolipids in senescence: Implication in aging and age-related diseases. *The Journal of Clinical Investigation*, *128*(7), 2702–2712. https://doi.org/10.1172/jci97949

Vaughen, J. P., Theisen, E., & Clandinin, T. R. (2023). From seconds to days: Neural plasticity viewed through a lipid lens. *Current Opinion in Neurobiology*, *80*, 102702. https://doi.org/10.1016/j.conb.2023.102702

Wake, H., Lee, P. R., & Fields, R. D. (2011). Control of local protein synthesis and initial events in myelination by action potentials. *Science*, *333*(6049), 1647–1651. https://doi.org/10.1126/science.1206998

Wang, L., Lin, G., Zuo, Z., Li, Y., Byeon, S. K., Pandey, A., & Bellen, H. J. (2022). Neuronal activity induces glucosylceramide that is secreted via exosomes for lysosomal degradation in glia. *Science Advances*, *8*(28), eabn3326. https://doi.org/10.1126/sciadv.abn3326

Wattenberg, B. W. (2019). Intra- and intercellular trafficking in sphingolipid metabolism in myelination. *Advances in Biological Regulation*, *71*, 97–103. https://doi.org/10.1016/j.jbior.2018.11.002

Xiao, L., Ohayon, D., McKenzie, I. A., Sinclair-Wilson, A., Wright, J. L., Fudge, A. D., Emery, B., Li, H., & Richardson, W. D. (2016). Rapid production of new oligodendrocytes is required in the earliest stages of motor-skill learning. *Nature Neuroscience*, *19*(9), 1210–1217. https://doi.org/10.1038/nn.4351

Xin, W., & Chan, J. R. (2020). Myelin plasticity: Sculpting circuits in learning and memory. *Nature Reviews. Neuroscience*, *21*, 682–694. https://doi.org/10.1038/s41583-020-00379-8

Yurlova, L., Kahya, N., Aggarwal, S., Kaiser, H. J., Chiantia, S., Bakhti, M., Pewzner-Jung, Y., Ben-David, O., Futerman, A. H., Brügger, B., & Simons, M. (2011). Self-segregation of myelin membrane lipids in model membranes. *Biophysical Journal*, *101*(11), 2713–2720. https://doi.org/10.1016/j.bpj.2011.10.026

Zöller, I., Büssow, H., Gieselmann, V., & Eckhardt, M. (2005). Oligodendrocyte-specific ceramide galactosyltransferase (CGT) expression phenotypically rescues CGT-deficient mice and demonstrates that CGT activity does not limit brain galactosylceramide level. *Glia*, *52*(3), 190–198. https://doi.org/10.1002/glia.20230

SUPPORTING INFORMATION

Additional supporting information can be found online in the Supporting Information section at the end of this article.

How to cite this article: Kato, D., Aoyama, Y., Nishida, K., Takahashi, Y., Sakamoto, T., Takeda, I., Tatematsu, T., Go, S., Saito, Y., Kunishima, S., Cheng, J., Hou, L., Tachibana, Y., Sugio, S., Kondo, R., Eto, F., Sato, S., Moorhouse, A. J., Yao, I., … Wake, H. (2023). Regulation of lipid synthesis in myelin modulates neural activity and is required for motor learning. *Glia*, *71*(11), 2591–2608. https://doi.org/10.1002/glia.24441

10981136, 2023, 11, Downloaded from https://onlinelibrary.wiley.com/doi/10.1002/glia.24441 by Kobe University, Wiley Online Library on [14/09/2023]. See the Terms and Conditions (https://onlinelibrary.wiley.com/terms-and-conditions) on Wiley Online Library for rules of use; OA articles are governed by the applicable Creative Commons License